Journal of Neuroinflammation

RESEARCH

Open Access

Semaglultide targets Spp1$^+$ microglia/macrophage to attenuate neuroinflammation following perioperative stroke

Yan Li[1,2†], Qiuyue Fan[1,2†], Rui Pang[1,2†], Ling Cai[1,2], Jie Qi[1,2], Weijie Chen[1,2], Yueman Zhang[1,2], Chen Chen[1,2*], Weifeng Yu[1,2*] and Peiying Li[1,2,3*]

Abstract

Peripheral surgery evokes neuroimmune activation in the central nervous system and modulates immune cell polarization in the ischemic brain. However, the phenotypic change of microglia and myeloid cells within post-surgical ischemic brain tissue remain poorly defined. Using an integrated approach that combines single-cell RNA sequencing with comprehensive biological analysis in a perioperative ischemic stroke (PIS) model, we identified a distinct Spp1-positive macrophage/microglia (Spp1$^+$ Mac/MG) subgroup that exhibit enriched anti-inflammatory pathways with distinct lipid metabolic reprogrammed profile. Moreover, using immunofluorescence staining, we identified the expression of Glucagon-like peptide-1 receptor (GLP1R) in Spp1$^+$F4/80$^+$ cells and Spp1$^+$Iba-1$^+$ cells. Intraperitoneal administration of semaglutide, a GLP1R agonist clinically approved for the treatment of type 2 diabetes mellitus, resulted in a significant reduction of cerebral infarct volume in PIS mice compared to that in ischemic stroke (IS) mice. Meanwhile, semaglutide treatment also increased the proportion of Spp1$^+$Edu$^+$Iba-1$^+$ cells 3 days after PIS. Using high-parameter flow cytometry, immunofluorescence staining and RNA sequencing, we demonstrated that semaglutide treatment significantly attenuated the expression of neuroinflammatory markers in mice following PIS. We also found that semaglutide treatment significantly ameliorated sensorimotor dysfunction up to 3 days after PIS in mice. Our current finding reveal a novel protective Spp1$^+$Mac/MG subset after PIS and demonstrated that it can be upregulated by semaglutide. We propose that targeting Spp1$^+$Mac/MG subsets using semaglutide could serve as a promising strategy to attenuate the exacerbated neuroinflammation in PIS.

Keywords Perioperative ischemic stroke, Spp1$^+$ Mac/MG, Semaglutide, Neuroinflammation

†Yan Li, Qiuyue Fan and Rui Pang contributed equally to this work.

*Correspondence:
Chen Chen
reallllicici@gmail.com
Weifeng Yu
ywf808@yeah.net
Peiying Li
peiyingli.md@gmail.com
[1]Department of Anesthesiology, Renji Hospital, Shanghai Jiao Tong University School of Medicine, Shanghai, China
[2]Key Laboratory of Anesthesiology, Shanghai Jiao Tong University, Ministry of Education, Shanghai, China
[3]Clinical Research Center, Renji Hospital, Shanghai Jiao Tong University School of Medicine, Shanghai, China

Introduction

Perioperative ischemic stroke (PIS) can elicit aggravated neuroinflammation and exacerbated neurological deficits [1–3]. Emerging evidence highlights peripheral surgical trauma as a potent driver of systemic inflammation and exacerbated neuroinflammation. The systemic immune activation disrupts cerebral immune homeostasis, inducing over activated neuroimmune responses characterized by blood-brain barrier (BBB) disruption and facilitates crosstalk between peripheral and brain-resident myeloid cells. The brain infiltrated macrophages and brain resident microglia can amplify neuroinflammatory cascades that worsen secondary neuronal damage [4, 5]. Our previous work demonstrated that peripheral surgical trauma activated peripheral myeloid cells, triggering the release of pro-inflammatory mediators (e.g., cytokines, chemokines) that exacerbated BBB disruption in murine models [6, 7]. Microglia mediated neuroinflammation in the injured brain are critical regulators of long-term neurological outcome by adopting neurodegeneration-specific transcriptional programs and exhibit transcriptionally distinct phenotypes of ischemic stroke-associated microglia and disease-associated microglia (DAM) [8–12]. Some specific microglia subsets, for example, DAM [12, 13], age-associated-microglia [14], $APOE^+$ microglia have been suggested to be involved not only in the brain injury evolving, but also long-term cognitive dysfunction [15–17]. Meanwhile, the brain infiltrated macrophages are also highly heterogenous. However, how does surgery induced systemic immune activation regulate the transcriptional heterogeneity and functional diversity of myeloid cells in the context of PIS remain largely unknown.

Recent studies have explored a plethora of myeloid cell phenotype modulation strategies, such as Trem2 [18–20], and glucagon-like peptide-1 receptor (GLP1R) agonists to improve neurological outcomes of neurodegenerative diseases [21]. It was reported that subsets of glia (e.g. microglia and astrocytes) and infiltrating macrophages could express GLP1R [22] and the activation of GLP1Rs on microglia could modulate the neuroinflammation and neuronal apoptosis in epilepsy [23]. Therefore, GLP1R agonist turns out to be novel targets to reduce microglia/macrophage activation [24, 25]. Semaglutide, developed for the treatment of type 2 diabetes, has been recently shown to have neuroprotective effects in an MCAO model and regulate microglial polarization [26–28]. Considering the increasing number of patients under the treatment of semaglutide, it would be intriguing to know whether it could affect the heterogeneity of myeloid cells and protect against the exacerbated neuroinflammation after PIS.

Here, using an in vivo PIS (surgery plus dMCAO) mouse model, we discover a distinct PIS associated disease-specific $Spp1^+$Mac/MG subset characterized with anti-inflammatory and distinct lipid metabolic reprogrammed profile. Moreover, we find that intraperitoneal injection of the GLP-1R agonist semaglutide at 30 nmol/kg at 2 h and 1 day can induce the proliferation of $Spp1^+Iba\text{-}1^+$ cells and ameliorate neuroinflammation and neurological deficits after PIS. The current finding reveals a novel protective $Spp1^+$Mac/MG subset that can be upregulated by semaglutide after PIS, proposing a highly translational therapy to attenuate neuroinflammation and neurological deficits following PIS.

Methods

Animals

Male C57/BL6 mice were acquired from Shanghai SLAC Laboratory Animals, which maintained in accordance with conventional laboratory settings (22 °C, a 12-h light–dark cycle, and free access to food and water). All studies were conducted in line with the Institutional Guide for the Care and Use of Laboratory Animals and were approved by Renji Hospital Institutional Animal Care and Use Committee. Surgeries and all outcome assessments were performed by investigators who were 'blinded' to experimental group assignments.

Murine focal cerebral ischemia model

Male and female C57/BL6 mice (8–10-week-old) were subjected to distal middle cerebral artery occlusion (dMCAO) as previously described [29]. Briefly, mice were anesthetized with 2% isoflurane in a 30% O2/68% N2O mixture under spontaneous breathing conditions. A skin incision was made at the neck and the left common carotid artery was exposed and ligated. After the neck incision was sutured, another skin incision was made between the left eye and ear. The temporal muscle was dissected, and a burr hole was opened to expose the distal part of middle cerebral artery occlusion (MCA). The dura mater was then cut, and the distal MCA was coagulated with low-intensity bipolar electrocautery (Shanghai Hutong Electronics Co. Ltd.) at the immediate lateral part of the rhinal fissure. Sham-operated animals underwent anesthesia and surgical exposure of arteries but without artery occlusion. Mice were sacrificed by high CO2 asphyxiation. The number of animals that received surgery was determined based on prior experimentation in our lab. All efforts were made to minimize animal suffering and the number of animals used.

Bone fracture surgery model

Twenty-four hours before the dMCAO procedure, animals were given general anesthesia with 2% isoflurane in a 30% O2/68% N2O mixture. Under aseptic surgical conditions, animals received an open tibia fracture of the right hindlimb with an intramedullary fixation, as

previously described [30]. Briefly, after shaving the overlying skin and disinfecting with 0.5% chlorhexidine gluconate and 70% isopropyl alcohol, a fracture of the tibial shaft was created under direct vision. A longitudinal incision was made through the skin and fascia lateral to the tibia to expose the bone. A 0.5 mm hole was drilled just above the proximal third of the tibia to insert an intramedullary 0.38 mm diameter stainless steel fixation wire. Subsequently, the fibula and the muscles surrounding the tibia were isolated, the periosteum stripped over a distance of 10 mm circumferentially and an osteotomy was performed with scissors at the junction of the middle and distal third of the tibia. The skin was sutured with 8 – 0 Prolene (Ethicon) and intra-operative fluid loss was replaced with 0.5 ml of subcutaneously injected normal saline. Animals were allowed to recover spontaneously from the anesthetic under warm conditions and received one intraperitoneal injection of buprenorphine (0.3 mg in 100 µl saline). The rectal temperature was maintained at 37 ± 0.5 °C using a thermal blanket throughout the surgical procedure. The tibia fracture surgery did not present any lethality.

Drug administration

Semaglutide was purchased from China peptides Ltd. Company (Shanghai, China). 0.2 mg semaglutide was dissolved with 531.2 µl PBS and stored as a stock with the concentration of 105 nmol/L. For injection, 7.5 µl stock was diluted with 192.5 µl PBS, and then injected into 25 g mouse (30nmol/kg) at 2 h and 1 day after dMCAO via intraperitoneal (i.p.) injection, followed by the same dose injection every 2 days. The control group received 200 µl of PBS i.p. injection 2 h after reperfusion, followed by the same dose injection every 2 days as described [28].

MAP2 and IgG staining

Infarct volume was evaluated by microtubule-associated protein 2 (MAP-2) immunofluorescence staining. BBB leakage was evaluated by extravasation of plasma IgG. We incubated the brain sections with primary antibodies against anti-MAP2(Rabbit monoclonal), followed by incubation with fluorescent secondary antibody Anti-Rabbit IgG H&L (Alexa Fluor® 594) and Anti-Mouse IgG H&L (Alexa Fluor® 488). The sections were then imaged using a confocal microscope, and the infarct volume or IgG^+ area was determined with NIH Image J (1.52a) analysis by an investigator who was blinded to the experimental group assignment.

Measurement of infarct volume

Brain slices were stained with 2,3,5-triphenyltetrazolium chloride (TTC, Sigma- Aldrich) as described [31]. TTC infarct area was determined with NIH ImageJ. Infarct volumes (with correction for brain edema) were calculated as the volume of the contralateral hemisphere minus the non-infarcted volume of the ipsilateral hemisphere.

Blood brain barrier disruption examination with Evans blue

Evans blue (EB, 4% in PBS, 4 ml/kg, Sigma-Aldrich) was intravenously injected, followed by 3 h of circulation before sacrifice. N, N-dimethylformamide was added to the brain tissue and the tissue was sonicated on ice for 1 min. EB levels in each hemisphere were determined as follows: {A620nm – [(A500nm + A740nm) / 2]} / mg wet weight. Background EB levels in the non-ischemic hemisphere were subtracted from those detected in the ischemic hemisphere [31].

Immunofluorescence staining

Coronal brain sections were subjected to immunofluorescence staining at indicated time points. Mice were sacrificed by high CO_2 asphyxiation. Brains were carefully extracted from the skull following transcardial perfusion with saline and 4% paraformaldehyde in phosphate-buffered saline (PBS). Brains were then dehydrated in 30% sucrose in PBS, and 25-µm thick brain sections were cut on a freezing microtome and subjected to immunofluorescent staining. Briefly, floating brain sections were blocked with 5% donkey serum in 0.3% Triton X-100 in PBS (PBST) for 1 h at room temperature (RT), followed by overnight incubation with primary antibodies at 4 °C. After three washes in 0.3% PBST, sections were incubated with the appropriate secondary antibodies for 1 h at RT. Sections were incubated in the following primary antibodies over-night at 4 °C: rabbit anti-MAP2 (Abcam), goat anti-CD31 (R&D), rabbit anti-ZO-1 (Proteintech), rabbit anti-Claudin5 (Abcam), rabbit anti-VE-cadherin (Abcam), rabbit anti-Spp1 (Abcam), goat anti-CD36 (Abcam), rat anti-F4/80 (Abcam), rabbit anti-GLP1R (Abcam), rabbit anti-Mki67 (Cell signaling technology). Confocal images were captured on a laser scanning confocal microscope (Olympus Fluoview FV3000, Olympus). Three randomly selected microscopic fields in cortex on each of three consecutive sections were analyzed for each brain by a blinded investigator.

Flow cytometry

For mice peripheral blood cells, single cell suspensions were prepared using RBC lysis buffer (BD Biosciences) and filtered through a 70 µm nylon membrane. Single cell suspensions were stained with anti-mouse CD45 (BD Biosciences), CD11b (BD Biosciences), F4/80 (BD Biosciences), Ly6G (BD Biosciences), NK1.1 (R&D), CD19 (BD Biosciences), CD11c (BD Biosciences), Spp1 (BD Biosciences), CD8 (BD Biosciences), CD4 (BD Biosciences) and appropriate isotype controls. The cell

number counted on the FACS Verse cell sorter (BD Biosciences) and analyzed using FlowJo software (Tree-Star). Dead cells were stained using the Live/Dead Fixable Blue Dead Cell Stain kit (1:1,000; Thermo Fisher Scientific, catalog no. L34962) and excluded from the analysis. Data analysis was performed using FlowJo v.10.5.3 (BD Biosciences). Doublets were excluded via FSC-A versus FSC-H gating. After gating on live $CD45^+$ cells, we performed multiple unbiased analyses with FlowJo, including generation of t-distributed stochastic neighbor embedding (t-SNE) plots for dimensionality reduction and data visualization, as well as PhenoGraphs to partition high-parameter single-cell data into subpopulations (clusters) based on phenotypic coherence. Cluster Explorer was used to visualize the PhenoGraph subpopulations on t-SNE plots. To identify clusters containing RAMs, we first identified microglia based on CD11b, and CX3CR1 expression, and then defined macrophage clusters based on CD11b, F4/80 expression.

RNA-sequencing

Samples were minced with a sterile scalpel into 1 mm^3 fragments, suspended in digestion buffer consisting of 1 mg/mL Collagenase type I (Sigma, C0130), 20U/mL Papain (Sigma, P4762), and 200U/mL DNase I (Worthington, LS006344) in HBSS (Solarbio, H1025), and incubated in a 37 °C water bath with shaking for 20 min. The suspension was passed through a 100 μm filter (Falcon, 3523260) and centrifuged (400 g, 10 min, 4 °C). Pelleted cells were resuspended in red blood cell lysis buffer (Solarbio, R1010), incubated for 2 min, passed through a 40 μm filter (Falcon, 3523240), collected by centrifugation (400 g, 10 min, 4 °C), and resuspended in pre-cooled solutions (Miltenyi Biotec, 130-093-634). Subsequently, the single-cell suspension was subjected to magnetic-activated cell sorting (MACS) to selectively enrich cells expressing the CD11b marker according to the manufacturer's protocol. Cells were manually counted using Trypan blue (Thermo, T10282) and AO-PI (LUNA, D23001) after each centrifugation (400 g, 10 min, 4 °C) and then resuspended. Total RNA from the cells was extracted using QIAGEN miRNeasy Micro Kit (Cat#217084, QIAGEN), and RNA quality was checked using Agilent 4200 TapeStation (Agilent technologies, Santa Clara, CA, US) according to standard procedures. Sequencing libraries were constructed by SMARTer Stranded Total RNA-Seq Kit for Illumina (Cat#634413, Takara) according to manufacturer's instructions. The sequencing was performed on an Illumina NovaSeq platform (Illumina, San Diego, CA, USA) and analyzed at Shanghai Biochip Co., Ltd., Shanghai, China.

Singlecell dissociation

scRNA-seq experiment was performed by experimental personnel in the laboratory of Biochip Co., Ltd. The brain tissues around infarction from PIS, IS and sham mice ($n = 3$/group) were surgically removed. We perfused the mice transcardially with ice-cold PBS before isolating brain tissues to obtain single-cell suspension. Cerebral infarction region of mouse was minced with a razor blade into 1 mm3 fragments, suspended in 5 ml of digestion buffer consisting of 2 mg/ml Papain (Sigma, P4762), 1 mg/mL Collagenase type II (Sigma, C6885) and 200U/ml DNase I (Worthington, LS006344) in RPMI medium (Coring, 10-040-CV), and incubated in 37℃ water bath with shaking for 45 min. The suspension was passed through a 100 μm filter (Falcon,3523260) and centrifugated (400 g, 10 min, 4℃). Pelleted cells were resuspended in red blood cell lysis buffer (Solarbio, R1010), incubated for 2 min, passed through a 40 μm filter (Falcon,3523240), collected by centrifugation (400 g, 10 min, 4℃) and resuspended in PBS (BI, 02-024-1ACS) containing 0.04% BSA (Sigma, B2064). Cells were manually counted by Trypan blue (Thermo, T10282) and AO-PI (LUNA, D23001) after each centrifugation (400 g, 10 min, 4℃) and resuspended. Single cells were processed using Chromium Controller (10X Genomics) according to the manufacturer's protocol.

Single-cell RNA sequencing

By using Chromium Next GEM Single Cell 3′ Kit v3.1 (10x Genomics, 1000268) and Chromium Next GEM Chip G Single Cell Kit (10x Genomics, 1000120), we performed single cell 3' gene expression profiling. The cell suspension was loaded onto the Chromium single cell controller (10x Genomics) to generate single-cell gel beads in the emulsion according to the manufacturer's protocol. Captured cells were lysed and the released RNA were barcoded through reverse transcription in individual GEMs. Cell-barcoded 3'gene expression libraries were sequenced on an Illumina NovaSeq6000 system by Shanghai Biochip Co., Ltd., Shanghai, China.

ScRNAseq statistical analysis

The raw reads were mapped to the mouse reference genome (refdata-gex-mm10-2020-A) using CellRanger count (v7.0.0) with default parameters, the digital expression matrix was extracted from the "filtered_feature_bc_matrix" folder outputted by the CellRanger count pipeline. The R package Seurat (v4.1.1) was performed to identify different clusters and signature genes. In brief, after removing genes expressed in fewer than 3 cells, cells with unique feature counts ranging from 300 to 6000 and less than 25% mitochondrial expression were selected for further analysis. We normalized raw data using NormalizeData function and extracted highly variable genes

using FindVariableFeatures function, then data integration was performed by canonical correlation analysis according to shared sources of variation across multiple datasets using SelectIntegrationFeatures, FindIntegrationAnchors and IntegrateData functions. The normalized data underwent linear transformation and principal component analysis based on highly variable genes using functions ScaleData and RunPCA. Graph-based clustering was performed according to the top 30 PCs using FindNeighbors and FindClusters with parameter "resolution = 0.5". RunUMAP was used to reduce the dimensions of the data, and the first 2 dimensions were used in plots. Meanwhile, the Wilcoxon rank-sum test was used to find differential expressed markers in each cluster by running FindMarkers function. Finally, we annotated each cell type by searching for specific gene expression pattern.

The Gene-Barcode matrices containing the barcoded cells and gene expression counts were imported into the Seurat R toolkit (R version 4.0.3 (2020-10-10)). Cells with gene number (6000) or high mitochondrial transcript ratio (> 25%), and genes expressed in less than 3 cells were all excluded. After removing unwanted cells from the dataset, all samples were combined with the function "merge". Next, we employed a global-scaling normalization method "LogNormalize" to normalize the feature expression measurements (UMI counts) for each cell by the total expression.

Highly variable genes (top 2000) were extracted to perform the principal component analysis (PCA) and top 30 of significant principal components were used for cluster analysis. Clusters were visualized using the Uniform Manifold Approximation and Projection (UMAP). Marker genes for each cluster, cell type and subgroup were identified by contrasting gene expression of cells from certain cluster, cell type or subgroup to that of others using the Seurat FindMarkers function. We performed unsupervised clustering of all brain cells and identified 28 distinct clusters. Peripheral leukocytes clusters are identified and subsetted based on expression of canonical gene signatures. Microglia clusters are identified and subsetted based on expression of canonical microglia gene signatures [2, 3]. Then, we further re-clustered all microglia and identified 8 microglia subclusters.

Pseudotime analysis

We applied Single-Cell Trajectories analysis using monocle3 (https://cole-trapnell.lab.github.io/monocle3) based on UMAP to estimate the pseudo-temporal path of microglia subclusters.

RNA velocity

Annotations of unspliced/spliced reads were obtained using velocyto CLI with default parameters. Reads were aligned to GENCODE reference build GRCm38.p6 release M23 with added tdTomato sequence. Next, we merged unspliced counts with the preprocessed, normalized, integrated and annotated (Seurat v4.0) spliced count matrix via the scvelo.utils.merge function and proceeded to the RNA velocity analysis using the velocyto (0.17) and scVelo (v0.2.4) workflow56. Briefly, before running the dynamical model, we computed moments for velocity estimation applying the values n_pcs = 20 and n_neighbors = 30 for the combined datasets from BM, blood, LN and CNS or n_pcs = 30 and n_neighbors = 30 for the CNS dataset. We ran the dynamical model to learn the full transcriptional dynamics of splicing kinetics, transcriptional state and cell-internal latent time across the complete dataset.

Pathway enrichment analysis

KEGG enrichment of cluster markers were performed using R package clusterProfiler (v4.4.4) with Benjamini-Hochberg multiple testing adjustment, using marker genes from Seurat software with wilcox test and log-scale foldchange (logfc.threshold > = 0.25).

EdU injections

To label cells that underwent proliferation, animals were intraperitoneally injected with the thymidine analog 5-ethynyl-2'-deoxy-uridine (EdU,50 mg/kg) at a concentration of 1 mg/ml in PBS twice a day (with an interval of at least 8 h). EdU administration was initiated on day 3 after dMCAO and continued for 3 consecutive days until day 5. Then samples were collected at indicated time points.

Evaluation of neurological function

The modified Garcia Score [32, 33], grid walk [34], and adhesive test [35] were performed to assess sensorimotor functions before and after surgery by investigators who were blinded to experimental group assignments. The modified Garcia Score is a well-established sensorimotor assessment system consisting of seven individual tests, of which one measures sensor function while four measure motor function. We scored each test from 0 to 3 (maximal score = 15): (a) body proprioception, (b) forelimb walking, (c) limb symmetry, (d) lateral turning, (e) climbing as described.

The grid walk test was performed according to Rogers et al. l [36] with slight modifications. Mice were placed on an elevated steel grid and foot faults (forelimb misplaced and slipping through the grid) were recorded during the moving process. Data are presented as percentage of foot faults for the right impaired forelimb referring to the total amount of right forelimb steps.

In the adhesive removal test, two adhesive tapes (0.3 × 0.4 cm) were placed on each paw. The order of placement of the adhesive (right or left) was random

in each animal and session. Then, the mouse was gently placed in a Perspex box, and the seconds to remove each adhesive tape were recorded. Mice were trained once daily before surgery for three consecutive days and regularly tested (three trails per day with 15 min interval of each mouse) after stroke at the indicated time points. The mean latency of three trails to touch and remove the tapes will be calculated.

Forelimb Grip strength testing was performed to assess forelimb grip strength using a digital grip strength meter. All tests were conducted in a quiet room to minimize stress on the animals. The grip strength meter was calibrated according to the manufacturer's instructions prior to use. The testing surface was cleaned to ensure optimal grip. Each mouse was gently grasped by the base of the tail using thumb and forefinger. The mouse was positioned horizontally over the grip strength meter with its forepaws making contact with the gripping surface. Only the forepaws were allowed to touch the meter while the body was held horizontal. The tail was then gently pulled back to encourage the mouse to grasp the meter. The maximum force exerted by the mouse when it released its grip was recorded in grams (g) or Newtons (N). Mice were trained once daily before surgery for three consecutive days and regularly tested (three trails per day with 15 min interval of each mouse) after stroke at the indicated time points. The maximum force from each trial was recorded, and the average grip strength was calculated for each animal.

Tyramide signal amplification (TSA) technique

The Tyramide Signal Amplification (TSA) technique is an enzymatic detection method that utilizes horseradish peroxidase (HRP) to label target proteins. It is analogous to conventional immunohistochemical methods, such as the DAB staining method, but includes enhanced signal amplification through the use of tyramide substrates. This methodology outlines the steps to perform TSA for the detection and visualization of specific proteins in tissue samples.

Incubate slides in blocking buffer for 1 h at room temperature to minimize non-specific binding. Apply the diluted primary antibody solution to the sections and incubate overnight at 4 °C in a humidified chamber to allow specific binding. Sections were incubated in the following primary antibodies over-night at 4 °C: rabbit anti-Spp1 (Abcam), rabbit anti-F4/80 (Abcam), rabbit anti-Iba-1 (CST), rabbit anti-GLRP1R (Abcam). Rinse the slides three times in wash buffer (PBS with 0.1% Tween-20) for 5 min each to remove unbound primary antibodies. Dilute the HRP-conjugated secondary antibodies in blocking buffer. Apply the diluted secondary antibodies to the tissue sections and incubate for 1 h at room temperature. Wash the sections three times in wash buffer for 5 min each. Apply the tyramide substrate solution to the slides and incubate for 10–30 min at room temperature, which activates the tyramide substrate. After incubation, rinse the sections briefly in wash buffer to remove excess tyramide substrate. For multiplex labeling, subject the slides to heat-induced epitope retrieval again to remove the non-covalently bound primary-secondary-HRP complexes from the previous round. This will help prepare the samples for additional antibody labeling. Wash the slides in PBS for 5 min. Repeat the previous steps involving primary and HRP-conjugated secondary antibodies, using additional primary antibodies specific to other targets and corresponding tyramide substrates. Ensure thorough washing between each step. After completing all necessary rounds, rinse the sections three times in wash buffer to eliminate unbound materials. Apply an appropriate mounting medium onto the slides and gently place coverslips over the samples. Allow the slides to dry completely before microscopy.

Gene set variation analysis (GSVA)

GSVA was performed using package "GSVA (v1.44.2)" in R, 50 hallmark gene sets used for analysis were retrieved from Molecular Signatures Database (MsigDB) using package "msigdbr (v7.5.1)". For each gene set, the average score of each cluster was calculated.

Statistical analysis

All statistics were performed using GraphPad Prism (v9.5.0) or the implemented statistical tests of the respective R pack ages. The Shapiro–Wilk normality test was initially performed on all data sets. A two-tailed Students t test was used for the pairwise comparison between two groups. For behavioral tests performed at multiple timepoints on the same animals, two-way ANOVA with repeated measures was used. The rest of the data were analyzed using a one-way or two-way ANOVA as appropriate. Multiple comparison procedures were carried out to identify specific between-group differences using post hoc Bonferroni's tests. Results were presented as mean ± SD. $P \leq 0.05$ was considered statistically significant. The number of samples is given in individual Figure legends and represent biological replicates, and individual values were plotted in figures. Sample sizes for animal studies were determined by power calculations for the primary parameter with mean differences and standard deviations based on pilot studies or the literature (power 80%, α 0.05). All raw data and results were interpreted in blinded fashion.

Results

Surgery induces pronounced change of F4/80$^+$Ly6G$^-$CD11b$^+$CD45$^+$and CD11b$^+$CD45^{int} cells in the ischemic brain

To examine the effect of surgery on the change of different cell types in the brain, we sorted cells from ischemic penumbra of 3 days in control (ctr), ischemic stroke (IS) and PIS mice and performed single cell RNA sequencing (scRNA seq) (Fig. 1A). Unsupervised clustering identified 28 subclusters, including monocytes (Mono, cluster 9,20), granulocytes (Granulo, cluster 22), oligodendrocytes (ODC, cluster 2,6,16,21,26,27), pericytes (cluster 7,17,25), endothelial cells (EC, cluster 0,3,4,14), smooth muscle cells (SMC, cluster 11), astrocytes (ASC, cluster 10,13,19), neuroblast (cluster 15,18), ependyma (cluster 24) on the basis of their signature genes 3 days after IS (Fig. 1B-C, Supplementary Fig. 1A). We next compared the cells compositional changes in the ischemic brain of IS and PIS mice. We found an increase of several immune cells, such as monocytes, granulocytes, microglia and a decrease of several brain resident cells, such as SMC, ASC, ependyma, pericytes and neuroblast in PIS mice compared to IS mice, while the increase of monocytes was the most prominent (Fig. 1D).

Next, we performed flow cytometry in the ctr, surgery alone, IS and PIS mice to further understand how the brain adjusted its immune response to exacerbate neuroinflammation in the PIS mouse brain. At 1 day after stroke, we found significantly increased F4/80$^+$Ly6G$^-$CD11b$^+$CD45$^+$ cells in the brain of PIS mice compared to IS, but not Ly6G$^+$CD11b$^+$CD45$^+$ cells (granulocytes), CD19$^+$CD11b$^+$CD45$^+$ cells (B cells), NK1.1$^+$CD45$^+$ cells (NK cells), or CD11c$^+$CD11b$^+$CD45$^+$ cells (DC cells) (Fig. 1E-F, Supplementary Fig. 2A-D); while at 3 days after stroke, the percentage of F4/80$^+$Ly6G$^-$CD11b$^+$CD45$^+$ cells and CD11b$^+$CD45^{int} cells significantly increased in the brains of PIS mice as compared to those of IS mice (Fig. 1E-H). The percentage of Ly6G$^+$CD11b$^+$CD45$^+$ cells (granulocytes), CD19$^+$CD11b$^+$CD45$^+$ cells (B cells, NK-1.1$^+$CD45$^+$ cells (NK cells), or CD11c$^+$CD11b$^+$CD45$^+$ cells (DC cells) remained unchanged in the brain of PIS mice compared to IS (Supplementary Fig. 2C-F). Notably, surgery alone did not significantly induce changes of inflammatory response in the brain parenchyma (Fig. 1E-F, Supplementary Fig. 2B-J). These results suggest that surgery induces increased infiltration of F4/80$^+$Ly6G$^-$CD11b$^+$CD45$^+$ cells in the CNS parenchyma of the ischemic brain and upregulates the number of CD11b$^+$CD45^{int} cells in the ischemic brain in PIS mice 3 days after stroke, which is consistent with our finding in scRNA seq.

At 3 days after stroke, we also found surgery induced larger infarct volume and increased BBB disruption in PIS mice than IS mice by 2,3,5-triphenyltetrazolium chloride (TTC) staining and Evans Blue (EB) extravasation, but not 1 day after stroke (Supplementary Fig. 3A-D). We further found that the sensorimotor function of the body proprioception, forelimb walking, limb symmetry, lateral turning, climbing, and total score as measured by modified Garcia score, grid-walking test, and adhesive removal test were significantly impaired in PIS mice as compared to IS mice up to 28 days after stroke, while surgery alone didn't elicit neurological dysfunction (Supplementary Fig. 4A-C). Collectively, these results suggest that surgery induces pronounced change of F4/80$^+$Ly6G$^-$CD11b$^+$CD45$^+$ and CD11b$^+$CD45^{int} cells in the ischemic brain.

Spp1$^+$ macrophages (Mac)/Microglia (MG) subsets emerge in the PIS mouse brain

To further understand the effect of surgery on the change of different subtypes of peripheral leukocytes in the brain, we subclustered peripheral immune cells into 9 clusters that were annotated by the expression of commonly used marker genes: mono/macs (Cd68,Lyz2:cluster0,1,8), neutrophils (S100a8,S100a9:cluster3), DCs (H2-Ab1,H2-Aa: cluster2,7), NKT cells (CD3g, Nkg7:cluster5), B cells (CD79a, CD79b: cluster6), mix cells (Slfn4,Btg2:cluster4) according to their signature genes and systematically compared the leukocyte compositional changes in the ischemic brain of IS of PIS mice (Fig. 2A-B). We found the number of macrophages (Macs) increased significantly in PIS mice as compared to that in IS mice (Supplementary Fig. 5A, Fig. 1E-F). The Mac1 subcluster exhibited the most pronounced expansion in PIS mice as compared to that in IS mice. Meanwhile the Mac1 subcluster was characterized by upregulated osteopontin (Spp1) - a gene associated with macrophage/microglial inflammatory responses and metabolic regulation(Fig. 2C) [37–40]. Thus, we define Mac1 as Spp1$^+$ Macs. Using immunohistochemistry staining and multiparametric flow cytometry analysis, we found a striking increase in the percentage of Spp1$^+$F4/80$^+$ cells among F4/80$^+$ cells CD11b$^+$CD45$^+$ cells or absolute number of Spp1$^+$F4/80$^+$ cells among CD11b$^+$CD45$^+$ cells in PIS mice compared to those in IS mice (Fig. 2D-F). While, cell numbers of Spp1$^+$CD4$^+$T cells, Spp1$^+$CD8$^+$T cells, Spp1$^+$DCs, Spp1$^+$B cells and Spp1$^+$granulocytes did not differ significantly among the ctr, IS and PIS groups (Supplementary Fig. 6). Since surgery or stroke could activate the host peripheral immune response, to determine whether the surgery or increases Spp1 expression in circulating myeloid, we next performed flow cytometry in the ctr, surgery alone, IS and PIS mice to further understand the change of Spp1 in circulating cells. We found that the percentage of Spp1$^+$F4/80$^+$CD11b$^+$CD45$^+$ cells of lymphocytes in blood were significantly increased in the surgery-alone group compared to that of control group

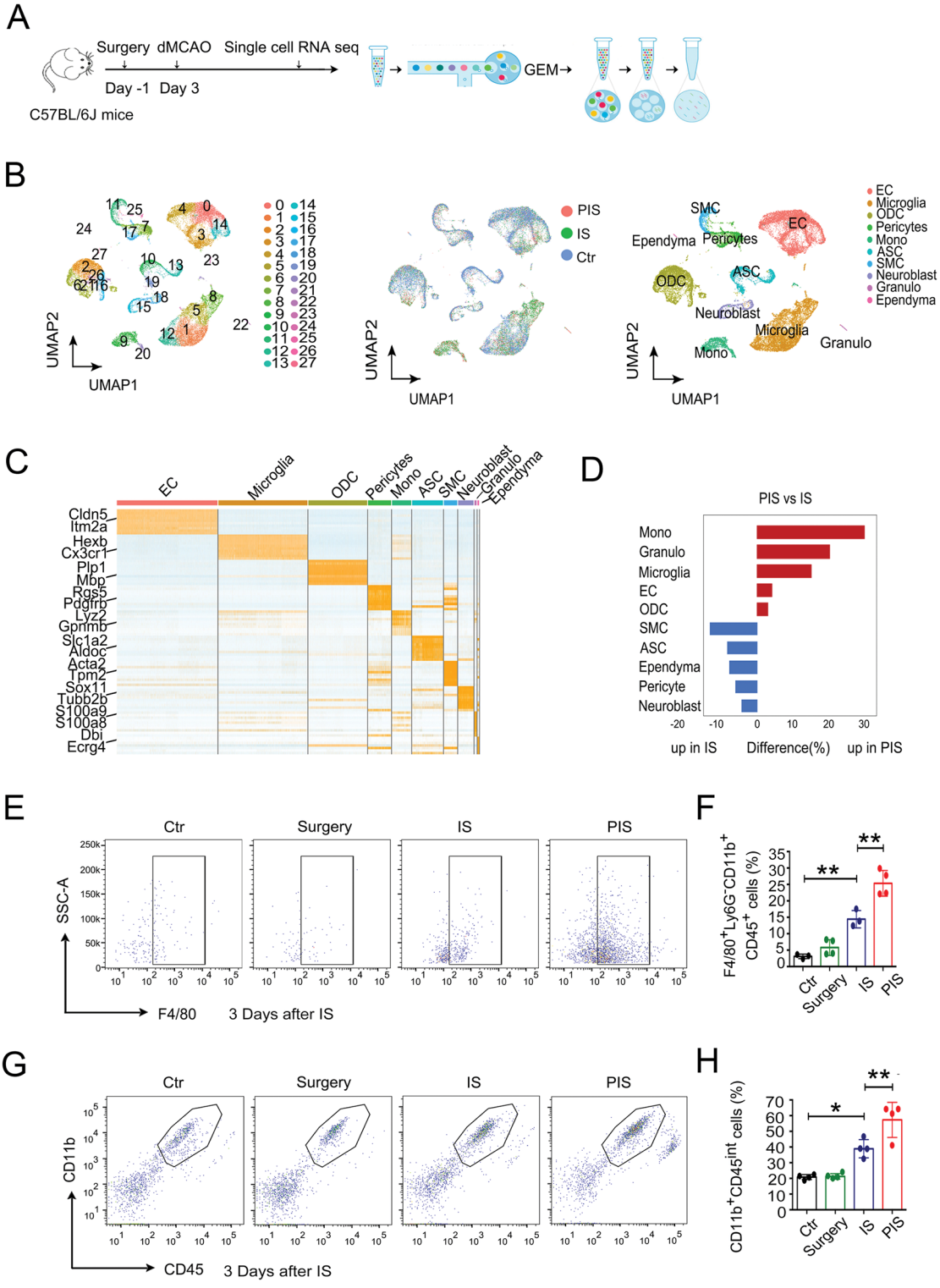

Fig. 1 (See legend on next page.)

(See figure on previous page.)

Fig. 1 Surgery induces pronounced F4/80$^+$Ly6G$^-$CD11b$^+$CD45$^+$ cells and CD11b$^+$CD45^{int} cells change in the ischemic brain. **A**. Diagram of experimental design. All cells were sequenced with a modified 10X chromium scRNA-seq procedure. **B**. UMAP representation of the 40,986 single cells shows the cellular heterogeneity of brain cells. Dots, individual cells; colors, cell clusters (left). UMAP representation of cells from 2 Ctr (n=14696 cells), 2 IS (n=12251 cells) and 2 PIS (n=14039 cells) mice brain. Dots, individual cells; colors, different origin (middle). UMAP representation of the 40,986 single cells shows the different cell types of brain cells. Dots, individual cells; colors, cell types (right). **C**. The heatmap of different expressed genes in different subclusters of cells in the above ischemic brain. **D**. Bi-directional histograms depict differences in relative cluster abundance between PIS and IS samples as shown in C. **E**. Flow cytometry analysis of F4/80$^+$Ly6G$^-$CD11b$^+$CD45$^+$ cells in the brain of Control (Ctr), Surgery, IS and PIS mice 3 d after dMCAO. **F**. Frequencies of F4/80$^+$Ly6G$^-$CD11b$^+$CD45$^+$ cells of tissue-resident leukocytes isolated out of the brain in E (n = 3–4 per group, one-way ANOVA with Bonferroni multiple comparisons test). **G**. Flow cytometry analysis of CD11b$^+$CD45^{int} cells in the brain of Ctr, Surgery, IS and PIS mice 3 d after dMCAO. **H**. Frequencies of CD11b$^+$CD45^{int} cells of tissue-resident leukocytes isolated out of the brain in E (n = 4 per group, one-way ANOVA with Bonferroni multiple comparisons test). Data are represented as mean ± SD. * $p \le 0.05$, ** $p \le 0.01$

(Supplementary Fig. 7A-B, E). The above changes were also found in PIS mice compared to that of IS alone group 3 d after dMCAO (Supplementary Fig. 7A-B, E). Interestingly, the percentage of Spp1$^+$F4/80$^+$CD11b$^+$CD45$^+$ cells among lymphocytes in blood exhibited a significant reduction in the PIS mice compared to that of surgery-alone group. Additionally, other immune cells in peripheral, such as granulocytes, NK cells, CD8$^+$ T cells and CD4$^+$ T cells expressed low level of Spp1 and remained unchanged between IS and PIS groups (Supplementary Fig. 7C-E). Thus, the peripheral surgery alone could induce the increases of Spp1$^+$F4/80$^+$ CD11b$^+$CD45$^+$ cells in the peripheral blood.

In addition to Macs, the percentage of MG also increases in the ischemic brain parenchyma in PIS mice compared to those in IS mice at 3 days after stroke (Fig. 1D, G-H). So, we next reclassified microglia and found eight distinct microglia subclusters, MG0–MG7 (Fig. 2G), which all expressed canonical microglia genes, including Hexb and Cx3cr1(Fig. 1C). We defined the above MG0 to MG7 subclusters using specific signatures as we previously reported [41–43] (Supplementary Fig. 8). Interestingly, MG4 also showed upregulation of Spp1, thus was defined as Spp1$^+$microglia (Spp1$^+$MG) (Fig. 2H). Multiparametric flow cytometry analysis revealed significantly increased cell number of Spp1$^+$CX3CR1$^+$CD11b$^+$CD45$^+$ cells in the ischemic brain of PIS mice as compared to that in ctr or IS alone mice (Fig. 2I-J). Collectively, these data revealed that surgery induced distinctive Spp1$^+$Mac/MG subsets emerged in the PIS mouse brain.

Spp1$^+$ Mac/MG subsets in the PIS mouse brain exhibit anti-inflammatory and lipid metabolic reprogrammed profile

We next characterized the transcriptional profile of Spp1$^+$Mac/MG subsets. Gene set variation analysis (GSVA) of peripheral immune cells revealed that Spp1$^+$Macs was scored the highest in the anti-inflammatory and lipid metabolic process signaling pathway (Fig. 3A). Several phagocytosis-associated genes in Spp1$^+$Macs were highly enriched, such as Ctsb, Ctsd, and Cd36 (Fig. 3B). Spp1$^+$Mac was also characterized by Arg1 expression (Fig. 3B), a gene associated with efferocytosis and anti-inflammatory function. KEGG pathway analysis revealed enriched pathways of oxidative phosphorylation, lysosome, and phagosome in Spp1$^+$Macs (Supplementary Fig. 5B). These findings suggest that Spp1$^+$Macs might be an anti-inflammatory subset with lipid metabolic reprogrammed profile. Next, we compared the transcriptional characteristics of these clusters with several previously defined populations under different pathological and physiological conditions, including inflammatory-macrophage, trem2^{high} macrophage, age-associated macrophage, stroke-associated myeloid cells (SAMC). We found that Spp1$^+$Macs were close to trem2^{high} macrophage, age-associated macrophages the SAMC (Fig. 3C). Collectively, these data revealed that Spp1$^+$Mac exhibits distinctive anti-inflammatory and lipid metabolic reprogrammed profile in the PIS mouse brain.

Using KEGG pathway analysis, we found that lysosome and phagosome pathways enriched in Spp1$^+$MG (Fig. 3D). It was shown that Spp1 was transiently expressed by specialized axon tract associated microglia (ATM) or damage associated microglia (DAM) in neurodegenerative diseases [42]. Next, we compared the transcriptional characteristics of these clusters with several previously defined populations under different pathological and physiological conditions. We found that Spp1$^+$MG exhibited a DAM/injury-responsive microglia (IRM)/ATM-like phenotype and resembling previously described BODIPY$^+$microglia and age-associated-MG (Fig. 3E). Immunohistochemistry staining confirmed the striking increase in the percentage of Arg1$^+$Spp1$^+$ Iba-1$^+$ cells and CD36$^+$Spp1$^+$ Iba-1$^+$ cells among Iba-1$^+$ cells in the ischemic penumbra in PIS mice compared with IS alone mice (Fig. 3F-G). Collectively, our data demonstrates that the Spp1$^+$ Mac/MG subset in the PIS mouse brain exhibits anti-inflammatory and lipid metabolic reprogrammed profile.

Proliferative Mki67$^+$MG can differentiate into Spp1$^+$MG in the PIS mouse brain

To further explore how does surgery lead to an increased number of Spp1$^+$ microglial after PIS, we analyzed the sc-RNA sequencing data of the PIS mouse brain. We

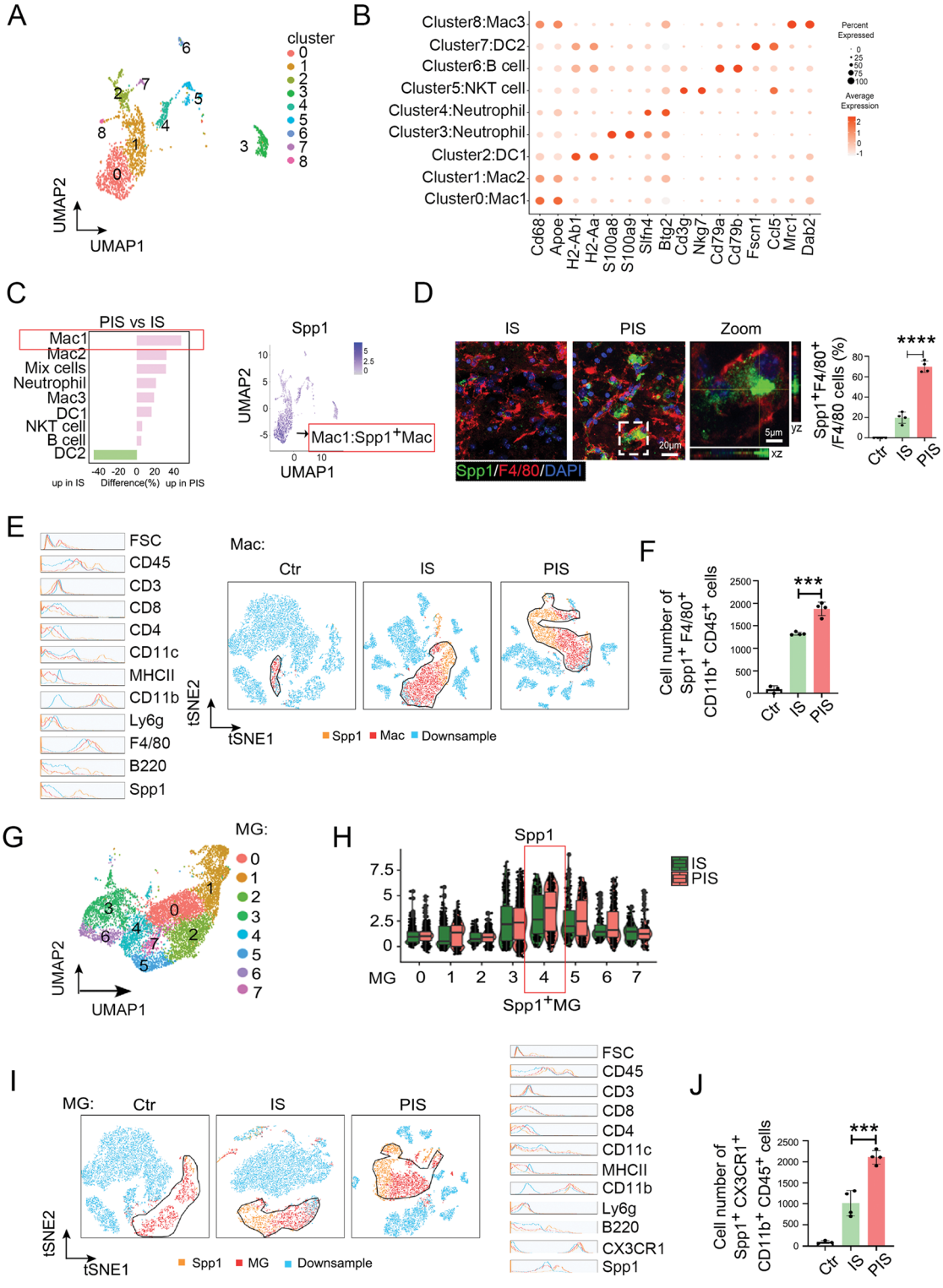

Fig. 2 (See legend on next page.)

(See figure on previous page.)

Fig. 2 Spp1$^+$ macrophages (Mac)/Microglia (MG) subsets emerged in PIS mouse brain. **A**. Uniform manifold approximation and projection (UMAP) representation of leukocytes in brain from Control (Ctr), IS, PIS mice 3 days after dMCAO for scRNA-seq colored by cell type (left) or sample (right). Each dot corresponds to one single cell. **B**. Dot plot of selected marker genes characterizing the clusters shown in A. The color of the dot indicates an average expression. **C**. Bi-directional histograms depict differences in relative cluster abundance between PIS and IS samples as shown in A (left). Feature Plots of selected marker genes (Spp1) specifically enriched in the Mac1 cluster (right). **D**. Representative images and statistical analysis of Spp1$^+$F4/80$^+$ cells of brain sections from Ctr, IS and PIS mice, as indicated 3 days after dMCAO. Scale bar: 20 μm. Zoom: Scale bar: 5 μm. Quantification of the percentage of Spp1$^+$Mac in the brain of each group ($n=4$ per group, one-way ANOVA with Bonferroni multiple comparisons test). **E**. t-distributed stochastic neighboring embedding (t-SNE) plots of high-parameter flow cytometry data of leukocytes extracted from brain of Ctr, IS and PIS mice at 3 days after dMCAO. Color coded by the epitope markers for F4/80$^+$macrophages (red), CD3$^+$ T cells (CD4$^+$ T cells and CD8$^+$ T cells), B220$^+$ B cells, CD11c$^+$ DCs, Ly6G$^+$ neutrophils and by Spp1 expression (orange) in leukocytes. ($n=4$ per group, one-way ANOVA with Bonferroni multiple comparisons test) (left). **F**. Comparison of Ctr, IS and PIS conditions reveals the high amounts of Spp1$^+$F4/80$^+$CD11b$^+$CD45$^+$ cells in brain from PIS compared with IS mice. ($n=4$ per group, one-way ANOVA with Bonferroni multiple comparisons test) (right). **G**. UMAP representation of microglia from brain tissues of Ctr, IS and PIS mice 3 days after dMCAO. Each dot corresponds to one single cell. **H**. Violin plot of Spp1 in all microglia clusters of IS and PIS mice. **I**. t-SNE plots of high-parameter flow cytometry data of leukocytes extracted from brain of Ctr, IS and PIS mice at 3 days after dMCAO. Color coded by the epitope markers for CX3CR1$^+$ microglia (red), CD3$^+$ T cells (CD4$^+$ T cells and CD8$^+$ T cells), B220$^+$ B cells, CD11c$^+$ DCs, Ly6G$^+$ neutrophils and by Spp1 expression (orange) in leukocytes. **J**. The absolute numbers of Spp1$^+$CX3CR1$^+$CD11b$^+$CD45$^+$ cells in brain as indicated groups. ($n=4$ per group, one-way ANOVA with Bonferroni multiple comparisons test). Data are represented as mean ± SD. *** $p \le 0.001$, **** $p \le 0.0001$

found that MG3 and MG6 showed the largest increase, which showed upregulation of cell cycle-related genes, including Mki67 and Top2a, thus was defined as proliferative microglia (Fig. 4A-C). Immunohistochemistry staining confirmed the striking increase in the number of Mki67$^+$MG in PIS mice compared with IS alone mice (Fig. 4D). Pseudotime analyses and RNA velocity were used to explore the differentiation trajectory of microglia subclusters after PIS. Interestingly, we found that proliferative microglia transited to Spp1$^+$MG and differentiation direction flowed from proliferative microglia to Spp1$^+$MG (Fig. 4E-F). In order to further address the relationship between Mki67$^+$MG and Spp1$^+$ MG, we used a systemic in vivo DNA labeling strategy with 5-ethynyl-2'-deoxyuridine (EdU) in PIS mice. We found that EdU were incorporated in Spp1$^+$Iba-1$^+$ cells in the ischemic stroke brain 3 days after PIS (Fig. 4G). These data suggest that proliferative MG could differentiate into Spp1$^+$ MG and surgery induce the Spp1$^+$MG proliferation in PIS mice.

GLP1R expression on Spp1$^+$Mac/MG subset provides a therapeutic target to attenuate the exacerbated neuroinflammation following PIS

It was previously shown that metabolic reprogramming can regulate the polarization of Mac/MG [44–46]. Since GLP1R is an intriguing metabolic therapeutic target emerging in recent years, we examined the expression of GLP1R in Spp1$^+$Mac/MG in the PIS mouse brain. Using immunohistochemistry staining, we found that GLP1R expressed in Spp1$^+$F4/80$^+$ cells and Spp1$^+$Iba-1$^+$ cells in ischemic penumbra in IS mice but have no expression in Mac/MG in Ctr mice (Fig. 5A-C). The percentage of Spp1$^+$F4/80$^+$ cells and Spp1$^+$Iba-1$^+$ cells in ischemic penumbra in PIS was significantly increased compared with IS alone (Fig. 5A-C). Furthermore, using flow cytometry, we found that the percentage of GLP1R$^+$Spp1$^+$ cells among CD45$^+$CD11b$^+$ cells was significantly increased in ischemic penumbra in PIS mice compared with IS alone (Fig. 5D-F). Additionally, other resident cells in brain, such as neuron (NeuN$^+$ cells), endothelial cells (CD31$^+$ cells) and astrocytes (GFAP$^+$ cells) expressed low level of GLP1R compared to Mac/MG (Iba-1$^+$ cells) in ischemic penumbra in PIS mice (Supplementary Fig. 9A-B).

To examine whether GLP1R could affect Spp1$^+$Mac/MG subsets in the ischemic brain, we administered the clinically widely used GLP1R agonists semaglutide after stroke (Fig. 6A). We found that intraperitoneal injection of the semaglutide at 30 nmol/kg at 2 h and 1 day after stroke [28] significantly increased the percentage of Spp1$^+$Edu$^+$ cells among Iba-1$^+$ cells as compared to the PBS control 3 days after stroke in PIS mice (Fig. 6B). Additionally, the number of Spp1$^+$Mac/MG in ischemic brains increased significantly after treatment with semaglutide in PIS mice as compared to the control mice treated with PBS (Fig. 6C-D). Conversely, Semaglutide administration reduced the percentage of Spp1$^+$F4/80$^+$CD11b$^+$CD45$^+$ cells among lymphocytes in peripheral blood compared to the control mice treated with PBS (Supplementary Fig. 10A-B).

To investigate whether semaglutide regulates the neuroinflammation in PIS, we isolated CD11b$^+$ cells from the ischemic brain of semaglutide treated or PBS treated mice 3 days after dMCAO for RNA-sequencing (Fig. 6E). KEGG analysis of DEGs indicated enrichment of immune response pathways, including PPAR signaling pathways, cytokine and cytokine receptor interaction pathway (Fig. 6F). Meanwhile, the treatment of semaglutide markedly increased the number of Arg1$^+$Mac/MG and reduced CD16$^+$Mac/MG in the PIS mouse brain as compared to that in the PBS treated PIS mouse brain (Fig. 6G-H). Additionally, immunohistochemistry staining revealed that the treatment of semaglutide markedly reduced the percentage of iNOS$^+$F4/80$^+$ cells or iNOS$^+$Iba-1$^+$ cells as compared to the PBS treatment in ischemic penumbra in both male (Fig. 6I-K) and female

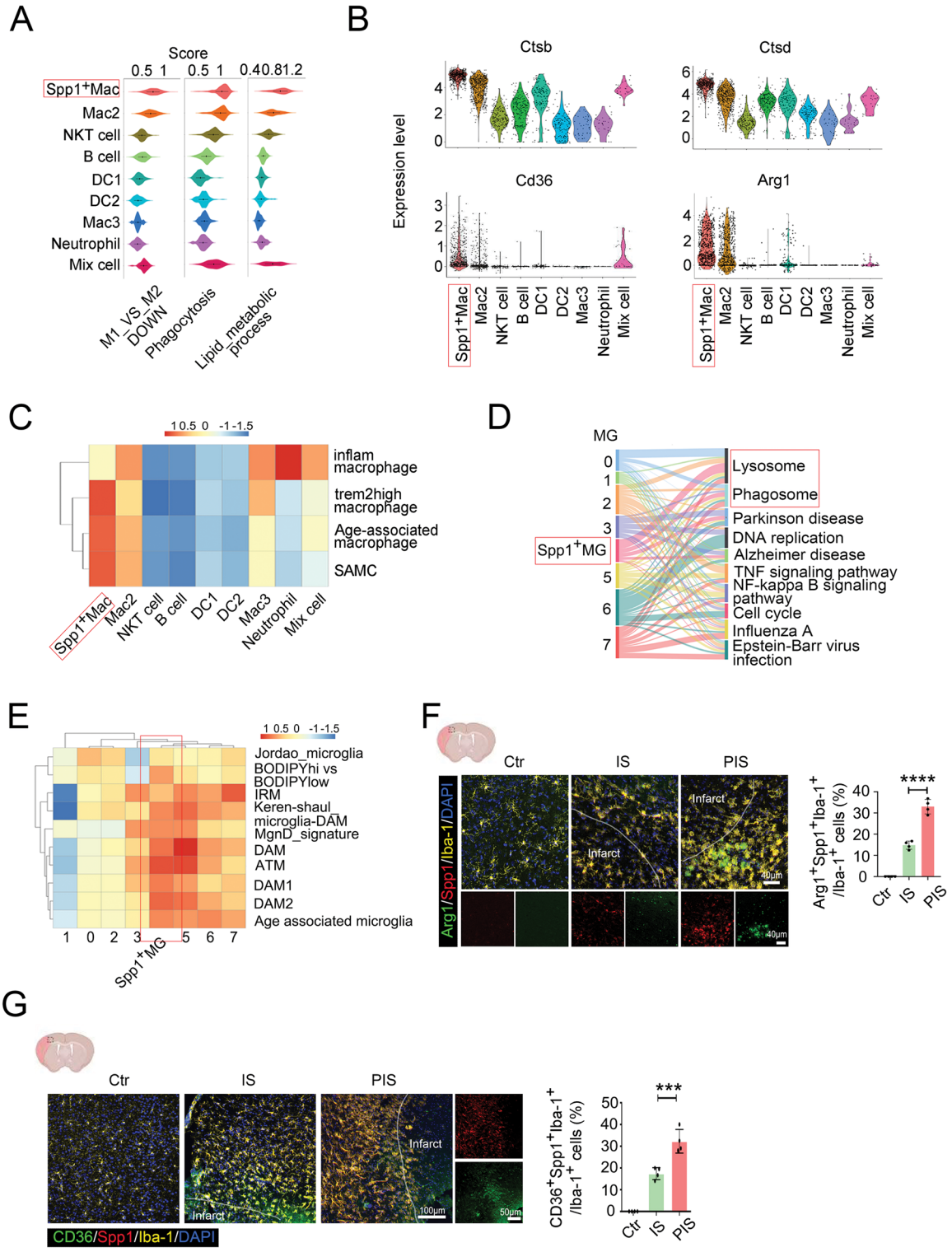

Fig. 3 (See legend on next page.)

(See figure on previous page.)

Fig. 3 Spp1$^+$Mac/MG subsets with similar characteristics in terms of inflammation, phagocytosis and lipid metabolic program. **A**. Gene set variation analysis (GSVA) of M1 vs. M2 down, Phagocytosis, Lipid metabolic process genes for each leukocyte. **B**. Violin plot of Ctsb, Ctsd, Cd36 and Arg1 in all leukocyte clusters. **C**. Heatmap showing the GSVA score of trem2high macrophage, Age-associated macrophage and the stroke-associated myeloid cell (SAMC) for each cluster defined as the average normalized expression of the pathway-related genes. See Additional file 1: Table 1 (a list of previously defined population genes under different pathological and physiological conditions) for a list of trem2high macrophage, Age-associated macrophage and the stroke-associated myeloid cell (SAMC) associated genes. **D**. Alluvial plot depicting the most affected KEGG for each cluster. Upregulated genes of each cluster were used for the enrichment analysis. Ribbon thickness indicates the number of genes per biological term. **E**. Heatmap showing the GSVA score of Jordao_microglia, BODIPYhi vs. BODIPYlow, IRM injury-responsive microglia (IRM), Keren-shaul_DAM, MgnD_signature, disease-associated microglia (DAM), axon tract associated microglia (ATM), DAM1, DAM2, Age-associated microglia for each cluster defined as the average normalize expression of the pathway-related genes. See Additional file 1: Table 1 (a list of previously defined population genes under different pathological and physiological conditions) for a list of associated genes. **F**. Representative confocal images of Arg1, Spp1 and Iba-1 triple immunostaining in the ischemic penumbra in Ctr, IS and PIS mice at 3days after dMCAO. Scale bar: 40 μm. Quantification of the percentage of Arg1$^+$Spp1$^+$Iba-1$^+$ cells in the brain of each group. ($n = 4$ per group, one-way ANOVA with Bonferroni multiple comparisons test). **G**. Representative confocal images of CD36, Spp1 and Iba-1 triple immunostaining in the ischemic penumbra in Ctr, IS and PIS mice at 3days after dMCAO. Scale bar: 40 μm. Quantification of the percentage of CD36$^+$Spp1$^+$ Iba-1$^+$ cells in the brain of each group. ($n = 4$ per group, one-way ANOVA with Bonferroni multiple comparisons test). The data are shown as means ± SD. ***$p \le 0.001$, **** $p \le 0.0001$

PIS mice (Supplementary Fig. 11A-C). Meanwhile, the treatment of semaglutide also increased the percentage of CD36$^+$Iba-1$^+$ cells as compared to the PBS treatment in ischemic penumbra in PIS mice (Supplementary Fig. 11D-E). These data suggest that targeting Spp1$^+$ Mac/MG using semaglutide could serve as a promising strategy to attenuate the exacerbated neuroinflammation following PIS.

Semaglutide reduces brain infarct volume and improves neurobehavioral outcomes after PIS

We next examined the effect of semaglutide on the brain injury and neurobehavioral outcomes following PIS. We found that both the infarct volume and the leakage of IgG were significantly reduced after treatment with semaglutide in PIS mice as compared to those treated with PBS treated mice (Fig. 7A-B). Meanwhile, the loss of ZO-1, Claudin-5 and VE-cadherin was reduced in the semaglutide treated mice as compared to that in the PBS treated PIS mice in ischemic penumbra (Fig. 7C-G). Consistently, the sensorimotor deficits measured by forelimb grip strength test were significantly improved in the semaglutide treatment group as compared to that in the PBS treated group (Fig. 7H). The above findings suggest that semaglutide can serve as a novel therapeutic strategy to reduce brain injury and improve neurobehavioral outcomes for PIS.

Discussion

Here, using single-cell transcriptional profiling, immunohistochemistry staining and multiparametric flow cytometry analysis, we discover a distinctive disease-specific Spp1$^+$ Mac/MG subsets in the ischemic brain after PIS. We find that Spp1$^+$ Mac/MG exhibits anti-inflammatory and lipid metabolic reprogrammed profile with increased expression of GLP1R. Treatment with semaglutide, a GLP1R agonist, results in increased proliferation of Spp1$^+$Iba-1$^+$ cells, an increased number of Spp1$^+$ Mac and reduced neuroinflammation in PIS mice.

Surgical trauma can stimulate the innate immune system and peripheral immune cells, which subsequently produce cytokines, such as TNF, IL-1β, IL-4 and IL-6 [47, 48], and then trigger additional neuroinflammatory processes and brain injury by activating microglia [49], especially under BBB disruption. In this study, we demonstrate that surgery induces pronounced inflammatory responses in the ischemic brain. Among the brain infiltrating immune cells, macrophages are the pronounced responder which participates in the innate immune response in the brain. Microglia, as the intrinsic immune cells of the CNS, shows a significant increase after surgery in the ischemic brain. However, it is still unclear how surgery influences the macrophages and microglia in the ischemic brain and thus affects the neurological function after PIS.

The identification of microglial or macrophage phenotypes that are associated with neuroinflammation in brain injury has sparked considerable interest in these cells [50–53]. With emerging findings using scRNA sequencing, several transcriptional profiles of microglia or macrophages were linked to the neuroinflammation, such as neurodegenerative disease-associated microglia, inflammation-associated macrophages, axon tract-associated microglia [10, 11, 42, 54]. It was previously reported that Spp1$^+$ Mac/MG were elevated in CNS and then counterbalanced the neuroinflammation and determined the progress of a variety of brain diseases [55–57]. Our previous study has found that macrophages are the most sensitive responder to surgery [6]. In this study, we found that surgery induces pronounced change of F4/80$^+$Ly6G$^-$CD11b$^+$CD45$^+$ and CD11b$^+$CD45^{int} cells in the ischemic brain in PIS mice compared to IS mice at 3 days after dMCAO. Although the CD11b$^+$CD45^{int} population in the post-ischemic brain should be considered a mixture of MG plus Mac that has undergone phenotype changes [58], the increased CD11b$^+$CD45^{int} cells in the brain after PIS arise from self-renewal of microglia or

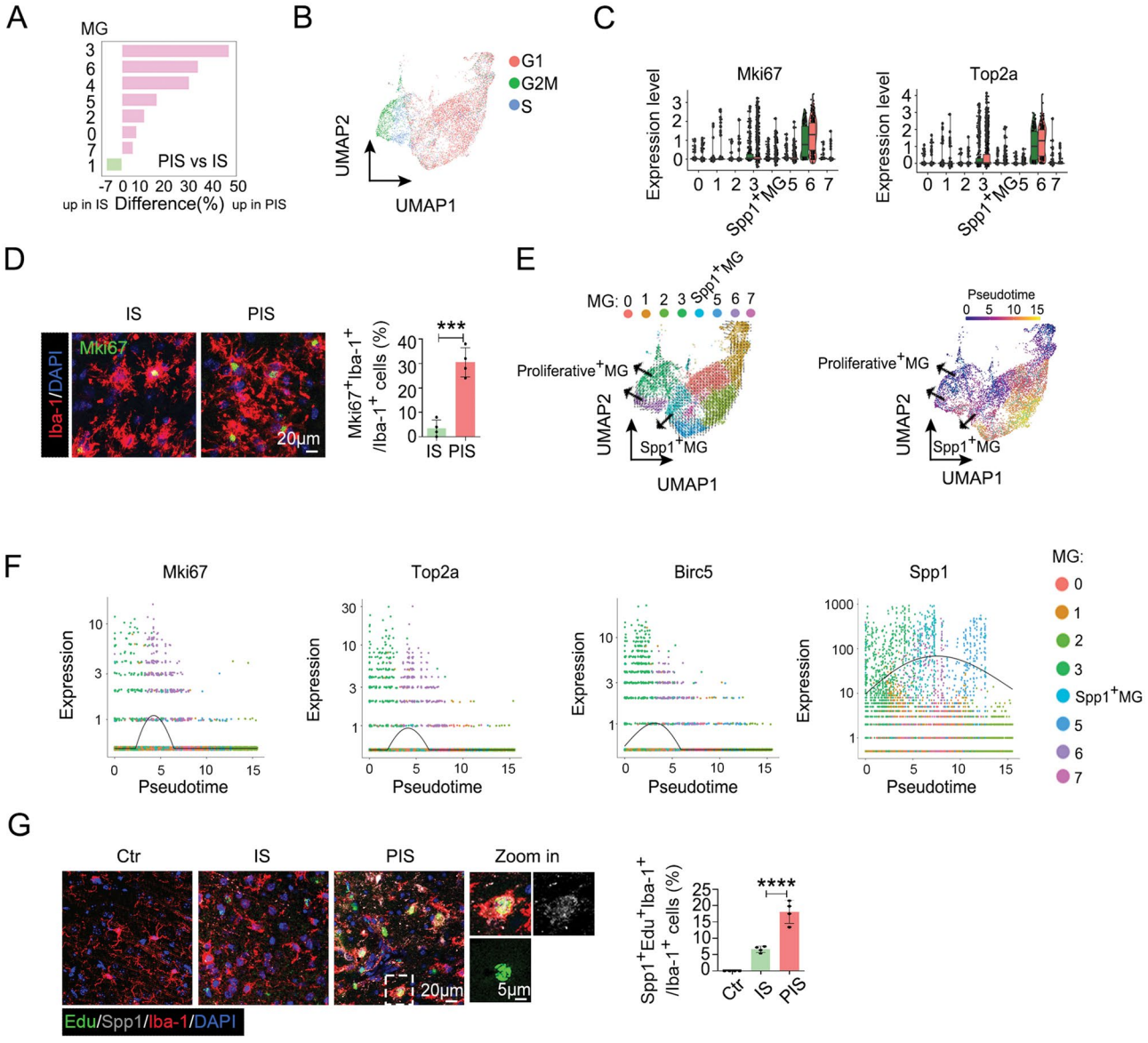

Fig. 4 Proliferative Mki67$^+$MG can differentiate into Spp1$^+$MG in PIS. **A**. Bi-directional histograms depict differences in microglia clusters abundance between PIS and IS samples as shown in Fig. 3**B**. UMAP displays cell cycle scores determined by expression of highly conserved cell cycle genes. **C**. Violin plot of Mki67, Top2a in all microglia clusters of IS and PIS mice. **D**. Representative confocal images of Mki67 and Iba-1 double immunostaining in the ischemic penumbra and quantification of the percentage of Mki67$^+$/ Iba-1$^+$ cells in IS and PIS mice at 3 days after tMCAO. Scale bar: 20 μm. ($n=4$ per group, unpaired Student's t test). **E**. Projection of pseudo-time generated with Monocle version 3 to infer the potential lineage differentiation trajectory onto the combined UMAP. From dark blue to yellow, indicating early and terminal states in the ischemic brain at different times after MCAO, respectively. **F**. Expression of selected genes (Mki67, Top2a, Birc5, Spp1) along pseudotime for microglia differentiation. **G**. Representative confocal images of Spp1, Iba-1 and EdU triple immunostaining in the ischemic penumbra in Ctr, IS and PIS mice at 3days after dMCAO. Scale bar: 20 μm. Zoom in: Scale bar: 5 μm. Quantification of the percentage of Spp1$^+$ Edu$^+$ Iba-1$^+$ cells in the brain of each group. ($n=4$ per group, one-way ANOVA with Bonferroni multiple comparisons test). Data are represented as mean ± SD. *** $p \le 0.001$, **** $p \le 0.0001$

conversion from infiltrating monocytes remains a critical question that warrants further investigation.

Additionally, Spp1$^+$ Mac accumulates significantly after surgery in PIS mice. Strikingly, surgery alone upregulate Spp1 level in F4/80$^+$Ly6G$^-$CD11b$^+$CD45$^+$ cells in blood, but not in neutrophil, NK cells or T cells, suggesting macrophages are the most sensitive responder to surgery to express Spp1. Interestingly, the percentage of Spp1$^+$F4/80$^+$ Ly6G$^-$CD11b$^+$CD45$^+$ cells in blood exhibited a significant reduction in the PIS mice compared to that of surgery-alone group, suggesting that peripheral Spp1$^+$F4/80$^+$ Ly6G$^-$CD11b$^+$CD45$^+$ cells may enter into ischemic brain when BBB damage. KEGG and GSVA analysis found that Spp1$^+$ Mac was enriched in

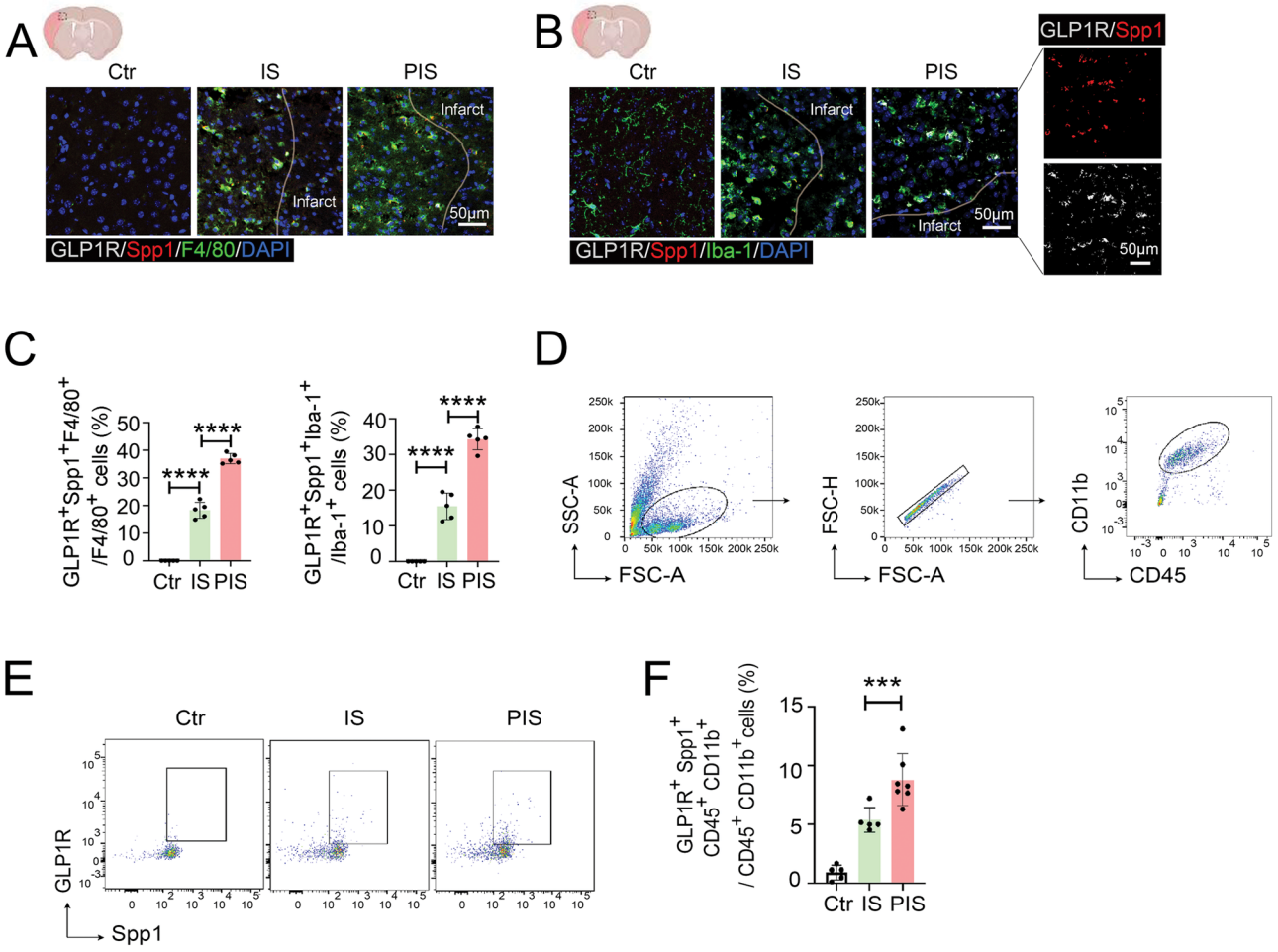

Fig. 5 The expression of GLP1R in Spp1$^+$ Mac/MG subpopulations increased in PIS mice. **A**. Representative confocal images of GLP1R$^+$ Spp1$^+$ F4/80$^+$ cells in ischemic penumbra in brain sections of indicated groups. Scale bar: 50 μm. **B**. Representative confocal images of GLP1R$^+$ Spp1$^+$ Iba-1$^+$ cells in ischemic penumbra in brain sections of indicated groups. Scale bar: 50 μm. **C**. Quantification of the percentage of GLP1R$^+$ Spp1$^+$ F4/80$^+$ cells (left) and GLP1R$^+$ Spp1$^+$ Iba-1$^+$ cells (right) in the brain of each group in A and B. ($n = 5$ per group, one-way ANOVA with Bonferroni multiple comparisons test). **D**. Gating strategy to identify CD45$^+$CD11b$^+$ cells by flow cytometry. **E**. Flow cytometry analysis of GLP1R$^+$Spp1$^+$CD45$^+$CD11b$^+$ cells isolated out of the brain from Ctr, IS and PIS mice 3 days after dMCAO. **F**. Frequencies of GLP1R$^+$Spp1$^+$ cells of CD45$^+$CD11b$^+$ cells isolated out of the brain from Ctr, IS and PIS mice 3 days after dMCAO analyzed by Flow cytometry. ($n = 5$–7 per group, one-way ANOVA with Bonferroni multiple comparisons test). The data are shown as means ± SD. ***$p \le 0.001$, **** $p \le 0.0001$

anti-inflammatory pathway, lipid metabolism pathway and with the high levels of phagocytosed-related genes, such as Ctsb, Ctsd, Cd36. Additionally, Arg1, a gene associated with efferocytosis and anti-inflammatory function, exhibits increased expression in Spp1$^+$Mac. Thus, Spp1$^+$Mac may be an anti-inflammatory subcluster with phagocytosis and metabolic program. We speculate that Spp1$^+$Macs may be protective macrophages to improve ischemic brain injury in PIS. Interestingly, we found that one microglia subcluster also expressed high levels of Spp1 in PIS mice and exhibited anti-inflammatory characteristics and enriched in phagocytosis and lipid metabolism pathway, which with similar characteristics to Spp1$^+$Mac. Additionally, the number of Spp1$^+$Iba-1$^+$CD45^{int} cells also increases significantly in PIS mice compared to IS mice and surgery induces Spp1$^+$Iba-1$^+$ cells proliferation in PIS mice. Interestingly, surgery along can't induce CD11b$^+$CD45^{int} cells in ischemic brain. However, proliferative Mki67$^+$ MG can differentiate into Spp1$^+$MG in the PIS mouse brain. We thus propose that the cerebral accumulation of Spp1$^+$Mac/MG subsets in PIS likely originates from both peripheral infiltration and central proliferation. Although some research reported that monocyte-derived macrophages, not microglia, exclusively express the proliferating marker Ki67 in the post-ischemic brain [58], it is well established that diverse immune cell populations exhibit significant heterogeneity in their functional states across distinct time points following stroke. Research has been dedicated to investigating microglial proliferation mechanisms at 3

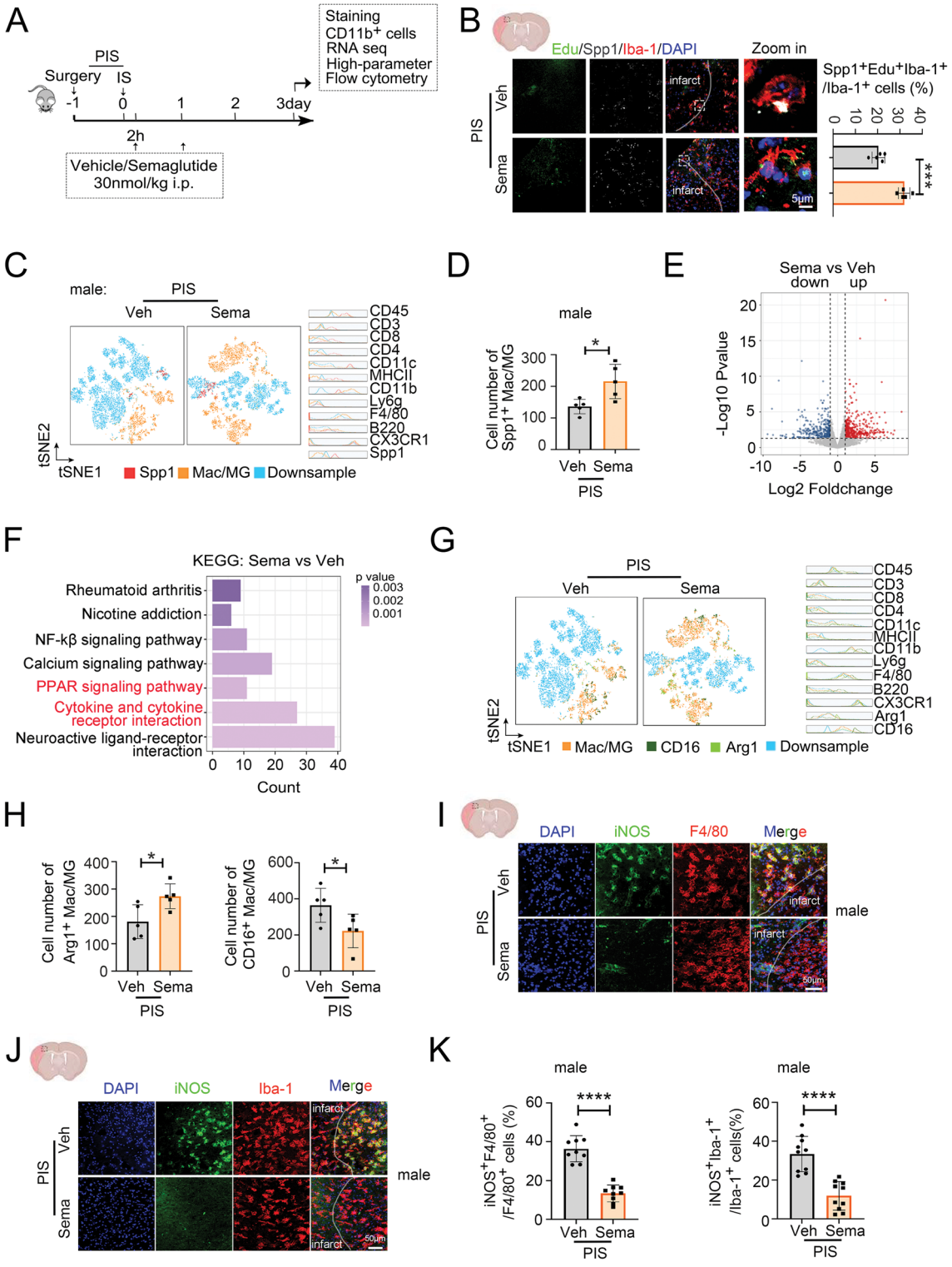

Fig. 6 (See legend on next page.)

(See figure on previous page.)

Fig. 6 Semaglutide increase the number of protective Spp1$^+$Mac/MG subpopulations and attenuate the neuroinflammation in PIS. **A**. The scheme of mice was administered PBS (Veh), semaglutide (Sema) after dMCAO in PIS mice. **B**. Representative confocal images (Left) and quantification (Right) of percentage of Spp1$^+$EdU$^+$ Iba-1$^+$ cells in ischemic penumbra in brain sections of indicated groups. Triangles indicate resident Spp1$^+$ Edu$^+$ Iba-1$^+$ cells. ($n=4$ per group, unpaired Student's t test). **C**. t-SNE plots of high-parameter flow cytometry data of leukocytes extracted from brain of mice administered Veh, Sema 3 days after dMCAO in PIS mice. Color coded by the epitope markers for CX3CR1$^+$ microglia and F4/80$^+$ macrophage (red), CD3$^+$T cells (CD4$^+$T cells and CD8$^+$T cells), B220$^+$B cells, CD11c$^+$ DCs, Ly6G$^+$neutrophils and by Spp1 expression (orange) in leukocytes. **D**. The absolute numbers of Spp1$^+$ Mac/MG in brain as indicated groups in C. ($n=4$ per group, unpaired Student's t test). **E**. Volcano plot showed the upregulated (red) and downregulated (blue) genes from RNA sequencing of CD11b$^+$ cells from of mice administered Veh, Sema 3 days after dMCAO in PIS mice. The horizontal axis is log2fold change, and the vertical axis is -log10p value, $p<0.05$. **F**. KEGG enrichment top 7 analysis suggested that PPAR signaling pathway and cytokine-cytokine receptor interaction were related with inflammation and the phenotypic changes of macrophage or microglia. **G**. t-SNE plots of high-parameter flow cytometry data of leukocytes extracted from brain of mice administered Veh, semaglutide (Sema) 3 days after dMCAO in PIS mice. Color coded by the epitope markers for CX3CR1$^+$microglia and F4/80$^+$macrophage (orange), CD3$^+$ T cells (CD4$^+$ T cells and CD8$^+$ T cells), B220$^+$ B cells, CD11c$^+$ DCs, Ly6G$^+$ neutrophils and Arg1 (light green) and CD16 (dark green) expression in leukocytes. **H**. The absolute numbers of Arg1$^+$ Mac/MG (left) and CD16$^+$ Mac/MG (right) in brain as indicated groups in G. ($n=4$ per group, unpaired Student's t test). **I**. Representative confocal images of the iNOS and F4/80 in ischemic penumbra in brain sections of indicated groups in male mice. Scale bar, 50 μm. **J**. Representative confocal images of the iNOS and Iba-1 in ischemic penumbra in brain sections of indicated groups in male mice. Scale bar, 50 μm. **K**. Quantification of percentage of iNOS$^+$F4/80$^+$ cells (left) and iNOS$^+$Iba-1$^+$ cells (right) in brain sections of indicated groups in I-J. ($n=9$ per group in male, $n=8$–9 per group in female, unpaired Student's t test). The data are shown as means ± SD. *$p \le 0.05$, ***$p \le 0.001$, **** $p \le 0.0001$

days post-stroke [59]. In our study, single-cell sequencing data revealed a proliferation-associated microglial phenotype in PIS at 3 days after dMCAO, characterized by high expression of the Mki67 gene. Crucially, microglia were distinguished from monocyte-derived macrophages through specific markers such as *Hexb* in single-cell analysis. These findings indicate that the observed proliferating cells are indeed resident microglia rather than infiltrating monocyte-derived macrophages. However, using fate mapping mice to further investigate the transition of microglia is necessary in future studies. Immunohistochemistry staining confirmed that Arg1 and CD36, which involvement of PPAR signaling pathway, exhibits increased expression in Spp1$^+$Iba-1$^+$ cells. Therefore, Spp1$^+$ Mac/MG could be an intriguing target to regulate the neuroinflammation after PIS.

GLP1 is a peptide hormone secreted by enteroendocrine cells, primarily intestinal L cells [60, 61]. GLP1 is primarily known for its role in glucose metabolism and appetite regulation [62, 63], but emerging research suggests that GLP1 also exerts significant effects on the immune system, particularly on macrophage function and phenotype [64–66]. GLP1 has been shown to promote the M2 phenotype in macrophages, enhancing their anti-inflammatory properties. This shift can lead to reduced production of pro-inflammatory cytokines (such as TNF-α and IL-6) and an increased anti-inflammatory cytokines (such as IL-10). By promoting the M2 phenotype, GLP1 can help regulate inflammation, potentially providing a therapeutic benefit in conditions characterized by chronic inflammation, such as obesity, diabetes, and cardiovascular diseases [64, 66, 67]. In this study, we found that microglia and macrophage express GLP1R, while other brain resident cells express low level of GLP1R. In PIS mice, the expression of GLP1R increases in Mac/MG in ischemic penumbra, compared to IS mice. The treatment of semaglutide increased Spp1$^+$Iba-1$^+$ cells proliferation in PIS mice and increases the number of Spp1$^+$CD11b$^+$CD45$^+$ cells in ischemic brain in PIS mice. To gain insight into the effect of semaglutide on neuroinflammation in PIS, transcriptomic analyses of CD11b$^+$ cells were performed. We found that cytokine and chemokine signaling pathways and PPAR signaling pathways were also enriched after semaglutide treatment. Additionally, semaglutide treatment markedly increases the number of Arg1$^+$ Mac/MG and reduces CD16$^+$ Mac/MG as compared to the PBS treated group in PIS mice in ischemic penumbra. The treatment of semaglutide also can improve brain injury and neurological dysfunction in PIS mice. From above data, we found that semaglutide exerts its protective effects through GLP1R expressed on Spp1$^+$ macrophages and microglia, which appear to be increased specifically in the ischemic penumbra. These results confirm that the treatment of semaglutide has great potential to be a protective therapy for PIS.

While our analysis unraveled a unique anti-inflammatory Spp1$^+$Mac/MG following ischemic stroke after surgery and proposes semaglutide as a potential therapeutic agent to mitigate surgery-related neuroinflammation, it has some limitations as follows. The detailed mechanisms of semaglutide on Spp1$^+$ Mac/MG subcluster is unclear. For example, how does semaglutide affect Arg1 or the PPAR signaling pathway in Spp1$^+$Mac/MG subcluster should be further investigated. Immunohistochemistry staining confirmed that the treatment of semaglutide increased Spp1$^+$Iba-1$^+$ cells proliferation in PIS mice. Using fate mapping mice to further investigate the mechanism of semaglutide on the activation Spp1$^+$Iba-1$^+$ cells proliferation is necessary. The absence of commercially available specific GLP-1R antagonists leading to limited understanding of the causal relationship between GLP1R and Spp1.Future studies using specific and targeted approaches to selectively eliminate or inactivate the GLP1R$^+$Mac/MG would be necessary to establish a

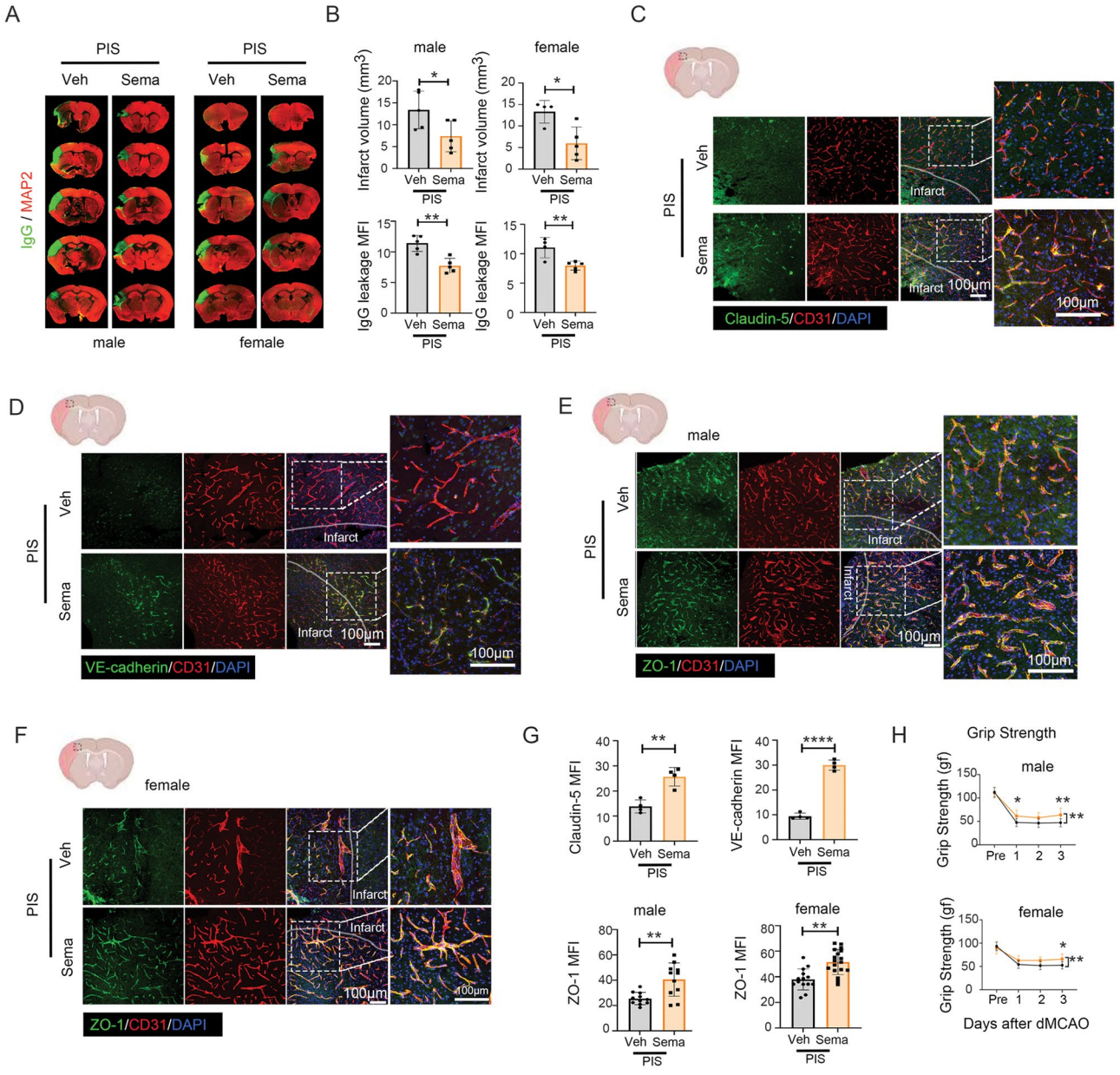

Fig. 7 Semaglutide reduces brain infarct injury and attenuates neurological dysfunction in PIS mice. **A**. Representative MAP2 staining (red) of brain infarct and endogenous mouse IgG staining (green) of BBB leakage of indicated groups in male (left) and female (right) mice. **B**. Quantification of infarct volume and IgG leakage of indicated groups in male (left) and female (right) mice. ($n = 4$–5 per group, unpaired Student's t test). **C**. Representative confocal images of the tight junction protein Claudin-5 and CD31 in brain sections of indicated groups in mice. Scale bar, 100 μm. Zoom in: Scale bar, 100 μm. **D**. Representative confocal images of the VE-cadherin and CD31 in brain sections of indicated groups in mice. Scale bar, 100 μm. Zoom in: Scale bar, 100 μm. **E**. Representative confocal images of the tight junction protein ZO-1 and CD31 in brain sections of indicated groups in male mice. Scale bar, 100 μm. Zoom in: Scale bar, 100 μm. **F**. Representative confocal images of the tight junction protein ZO-1 and CD31 in brain sections of indicated groups in female mice. Scale bar, 100 μm. Zoom in: Scale bar, 100 μm. **G**. Quantification of Claudin-5 mean fluorescence intensity (MFI) of indicated groups in C. ($n = 4$ per group, unpaired Student's t test). Quantification of VE-cadherin MFI of indicated groups in D. ($n = 4$ per group, unpaired Student's t test). Quantification of ZO-1 MFI of indicated groups in E. ($n = 11$ per group in male, unpaired Student's t test). Quantification of ZO-1 MFI of indicated groups in F. ($n = 14$–18 per group in female, unpaired Student's t test). **H**. Sensorimotor dysfunction after PIS in vehicle-treated and semaglutide-treated mice assessed by grip strength test (male: left; female: right). ($n = 10$ per group. two-way ANOVA with Bonferroni multiple comparisons test. The data are shown as means ± SD. $^{*}p < 0.05$, $^{**}p < 0.01$, $^{***}p \leq 0.001$, $^{****}p \leq 0.0001$

causal relationship between GLP1R activation by semaglutide and the induction of Spp1⁺MG.

Collectively, the current study reveals a unique anti-inflammatory Spp1⁺ Mac/MG evolution in ischemic brain after surgery. Targeting Spp1⁺Mac/MG subcluster, such as using semaglutide, can serve as promising therapeutic targets for attenuating neuroinflammation in CNS pathologies promoted by peripheral inflammation following PIS.

Supplementary Information

The online version contains supplementary material available at https://doi.org/10.1186/s12974-025-03465-9.

Supplementary Material 1

Supplementary Material 2

Supplementary Material 3

Supplementary Material 4

Acknowledgements
Not applicable.

Author contributions
Y.L., Q.F., C.C. and R.P. performed the experiments. L.C., J.Q., W.C., and Y.Z. analyzed the data. Y.L.and P.L. wrote the manuscript. Q.F., C.C., W.Y. and P.L. revised the manuscript. Y.L. and P.L. designed and supervised the study.

Funding
P.L. is supported by the National Natural Science Foundation of China (NSFC, U22A20295, W2411087, 91957111, 81971096, 82061130224, M-0671), New Frontier Technology Joint Research sponsored by Shanghai Shenkang Hospital Development Center (SHDC12019102), Shanghai Municipal Education Commission-Gaofeng Clinical Medical Grant Support (20181805), "Shuguang Program" supported by Shanghai Education Development Foundation and Shanghai Municipal Education Commission (20SG17), Newton Advanced Fellowship grant provided by the UK Academy of Medical Sciences (NAF\R11\1010), Innovative Research Team of High-level Local Universities in Shanghai (SHSMU-ZLCX20211602). Y.L. is supported by the National Natural Science Foundation of China (NSFC, 82401524), Shanghai "Science and Technology Innovation Action Plan" Natural Science Foundation (24ZR1444700). The study is supported by the Fundamental Research Funds for the Central Universities (No. 24×010202059), Shanghai Engineering Research Center of Peri-operative Organ Support and Function Preservation (No. 20DZ2254200).

Data availability
No datasets were generated or analysed during the current study.

Declarations

Ethical approval
Not applicable.

Consent for publication
Not applicable.

Competing interests
The authors declare no competing interests.

Received: 26 March 2025 / Accepted: 10 May 2025
Published online: 27 May 2025

References

1. Gelderblom M, et al. Temporal and Spatial dynamics of cerebral immune cell accumulation in stroke. Stroke. 2009;40(5):1849–57.
2. Zhou L, et al. Treatment of cerebral ischemia by disrupting ischemia-induced interaction of nNOS with PSD-95. Nat Med. 2010;16(12):1439–43.
3. Collaborators GBDN. Global, regional, and National burden of neurological disorders, 1990–2016: a systematic analysis for the global burden of disease study 2016. Lancet Neurol. 2019;18(5):459–80.
4. Hao H, et al. Inhibition of Bruton's tyrosine kinase restricts neuroinflammation following intracerebral hemorrhage. Theranostics. 2025;15(2):494–508.
5. Pocock JM, Piers TM. Modelling microglial function with induced pluripotent stem cells: an update. Nat Rev Neurosci. 2018;19(8):445–52.
6. Li Y, et al. Myeloid-derived MIF drives RIPK1-mediated cerebromicrovascular endothelial cell death to exacerbate ischemic brain injury. Proc Natl Acad Sci U S A. 2023;120(5):e2219091120.
7. Xuan W, et al. Dualistic roles and mechanistic insights of macrophage migration inhibitory factor in brain injury and neurodegenerative diseases. J Cereb Blood Flow Metab. 2023;43(3):341–56.
8. Zhang Y, et al. Novel CH25H(+) and OASL(+) microglia subclusters play distinct roles in cerebral ischemic stroke. J Neuroinflammation. 2023;20(1):115.
9. Garcia-Bonilla L, et al. Analysis of brain and blood single-cell transcriptomics in acute and subacute phases after experimental stroke. Nat Immunol. 2024;25(2):357–70.
10. Beuker C, et al. Stroke induces disease-specific myeloid cells in the brain parenchyma and Pia. Nat Commun. 2022;13(1):945.
11. Krasemann S, et al. The TREM2-APOE pathway drives the transcriptional phenotype of dysfunctional microglia in neurodegenerative diseases. Immunity. 2017;47(3):566–e5819.
12. Tian Z, Ji X, Liu J. Neuroinflammation in vascular cognitive impairment and dementia: current evidence, advances, and prospects. Int J Mol Sci, 2022. 23(11).
13. Chung HY, et al. Microglia mediate neurocognitive deficits by eliminating C1q-tagged synapses in sepsis-associated encephalopathy. Sci Adv. 2023;9(21):eabq7806.
14. Androvic P, et al. Decoding the transcriptional response to ischemic stroke in young and aged mouse brain. Cell Rep. 2020;31(11):107777.
15. Kaji S, et al. Apolipoprotein E aggregation in microglia initiates Alzheimer's disease pathology by seeding beta-amyloidosis. Immunity. 2025;58(1):263.
16. Rao A, et al. Microglia depletion reduces human neuronal APOE4-related pathologies in a chimeric Alzheimer's disease model. Cell Stem Cell. 2025;32(1):86–e1047.
17. Kaji S, et al. Apolipoprotein E aggregation in microglia initiates Alzheimer's disease pathology by seeding beta-amyloidosis. Immunity. 2024;57(11):2651–e266812.
18. Rachmian N, et al. Identification of senescent, TREM2-expressing microglia in aging and Alzheimer's disease model mouse brain. Nat Neurosci. 2024;27(6):1116–24.
19. Tagliatti E, et al. Trem2 expression in microglia is required to maintain normal neuronal bioenergetics during development. Immunity. 2024;57(1):86–e1059.
20. Yoo Y, et al. A cell therapy approach to restore microglial Trem2 function in a mouse model of Alzheimer's disease. Cell Stem Cell. 2023;30(8):1043–e10536.
21. Yun SP, et al. Block of A1 astrocyte conversion by microglia is neuroprotective in models of Parkinson's disease. Nat Med. 2018;24(7):931–8.
22. Cui QN, et al. The role of glia in the physiology and Pharmacology of glucagon-like peptide-1: implications for obesity, diabetes, neurodegeneration and glaucoma. Br J Pharmacol. 2022;179(4):715–26.
23. Zhang K, et al. Targeting microglial GLP1R in epilepsy: A novel approach to modulate neuroinflammation and neuronal apoptosis. Eur J Pharmacol. 2024;981:176903.
24. Lawrence ECN, et al. Topical and systemic GLP-1R agonist administration both rescue retinal ganglion cells in hypertensive glaucoma. Front Cell Neurosci. 2023;17:1156829.
25. Chen J, et al. Glucagon-Like Peptide-1 receptor regulates macrophage migration in monosodium Urate-Induced peritoneal inflammation. Front Immunol. 2022;13:772446.
26. Ahren B, et al. Efficacy and safety of once-weekly semaglutide versus once-daily sitagliptin as an add-on to Metformin, Thiazolidinediones, or both, in patients with type 2 diabetes (SUSTAIN 2): a 56-week, double-blind, phase 3a, randomised trial. Lancet Diabetes Endocrinol. 2017;5(5):341–54.
27. Sorli C, et al. Efficacy and safety of once-weekly semaglutide monotherapy versus placebo in patients with type 2 diabetes (SUSTAIN 1): a double-blind,

randomised, placebo-controlled, parallel-group, multinational, multicentre phase 3a trial. Lancet Diabetes Endocrinol. 2017;5(4):251–60.
28. Zhang Q, et al. Blocking C3d(+)/GFAP(+) A1 astrocyte conversion with semaglutide attenuates Blood-Brain barrier disruption in mice after ischemic stroke. Aging Dis. 2022;13(3):943–59.
29. Mracsko E, et al. Antigen dependently activated cluster of differentiation 8-positive T cells cause perforin-mediated neurotoxicity in experimental stroke. J Neurosci. 2014;34(50):16784–95.
30. Degos V, et al. Bone fracture exacerbates murine ischemic cerebral injury. Anesthesiology. 2013;118(6):1362–72.
31. Mao L, et al. Regulatory T cells ameliorate tissue plasminogen activator-induced brain haemorrhage after stroke. Brain. 2017;140(7):1914–31.
32. Cekanaviciute E, et al. Astrocytic transforming growth factor-beta signaling reduces subacute neuroinflammation after stroke in mice. Glia. 2014;62(8):1227–40.
33. Doyle KP, et al. Distal hypoxic stroke: a new mouse model of stroke with high throughput, low variability and a quantifiable functional deficit. J Neurosci Methods. 2012;207(1):31–40.
34. Rogers DC et al. Correlation between motor impairment and infarct volume after permanent and transient middle cerebral artery occlusion in the rat. Stroke, 1997. 28(10): p. 2060-5; discussion 2066.
35. Bouet V, et al. The adhesive removal test: a sensitive method to assess sensorimotor deficits in mice. Nat Protoc. 2009;4(10):1560–4.
36. Rogers D et al. Correlation between motor impairment and infarct volume after permanent and transient middle cerebral artery occlusion in the rat. Stroke, 1997. 28(10): p. 2060-5; discussion 2066.
37. Lawrence AR, et al. Microglia maintain structural integrity during fetal brain morphogenesis. Cell. 2024;187(4):962–e98019.
38. Lan Y, et al. Fate mapping of Spp1 expression reveals age-dependent plasticity of disease-associated microglia-like cells after brain injury. Immunity. 2024;57(2):349–e3639.
39. Loosen SH, et al. Elevated levels of Circulating osteopontin are associated with a poor survival after resection of cholangiocarcinoma. J Hepatol. 2017;67(4):749–57.
40. Bill R, et al. CXCL9:SPP1 macrophage Polarity identifies a network of cellular programs that control human cancers. Science. 2023;381(6657):515–24.
41. Young AMH, et al. A map of transcriptional heterogeneity and regulatory variation in human microglia. Nat Genet. 2021;53(6):861–8.
42. Hammond TR, et al. Single-Cell RNA sequencing of microglia throughout the mouse lifespan and in the injured brain reveals complex Cell-State changes. Immunity. 2019;50(1):253–e2716.
43. Rosin JM, et al. A subpopulation of embryonic microglia respond to maternal stress and influence nearby neural progenitors. Dev Cell. 2021;56(9):1326–e13456.
44. Zhong X, et al. Cordycepin modulates microglial M2 polarization coupled with mitochondrial metabolic reprogramming by targeting HKII and PDK2. Adv Sci (Weinh). 2024;11(31):e2304687.
45. Yao C, et al. rTM reprograms macrophages via the HIF-1alpha/METTL3/PFKM axis to protect mice against sepsis. Cell Mol Life Sci. 2024;81(1):456.
46. Gong L, et al. Metabolic reprogramming in gliocyte Post-cerebral ischemia/reperfusion: from pathophysiology to therapeutic potential. Curr Neuropharmacol. 2024;22(10):1672–96.
47. Didem B, et al. Early effects of laparotomy and laparoscopy on bacterial behavior and Proinflammatory cytokines on bacterial peritonitis in rats I: Escherichia coli. J Pediatr Surg. 2008;43(8):1494–501.
48. Yang T, Velagapudi R, Terrando N. Neuroinflammation after surgery: from mechanisms to therapeutic targets. Nat Immunol. 2020;21(11):1319–26.
49. Geloso MC, Zupo L, Corvino V. Crosstalk between peripheral inflammation and brain: focus on the responses of microglia and astrocytes to peripheral challenge. Neurochem Int. 2024;180:105872.
50. Willis EF, et al. Repopulating microglia promote brain repair in an IL-6-Dependent manner. Cell. 2020;180(5):833–e84616.
51. Abdelbasset M, et al. Differential contributions of fetal mononuclear phagocytes to Zika virus neuroinvasion versus neuroprotection during congenital infection. Cell. 2024;187(26):7511–e753220.
52. Sun S, et al. CHIT1-positive microglia drive motor neuron ageing in the primate spinal cord. Nature. 2023;624(7992):611–20.
53. Peruzzotti-Jametti L, et al. Mitochondrial complex I activity in microglia sustains neuroinflammation. Nature. 2024;628(8006):195–203.
54. Keren-Shaul H, et al. A unique microglia type associated with restricting development of Alzheimer's disease. Cell. 2017;169(7):1276–e129017.
55. Tang Y, et al. Single-cell RNA sequencing reveals the CRTAC1(+) population actively contributes to the pathogenesis of spinal ligament degeneration by SPP1(+) macrophage. Aging Cell. 2024;23(12):e14320.
56. Jie H, et al. Uncovering SPP1(+) macrophage, neutrophils and their related diagnostic biomarkers in intracranial aneurysm and subarachnoid hemorrhage. J Inflamm Res. 2024;17:8569–87.
57. Dufour A, et al. Neonatal inflammation impairs developmentally-associated microglia and promotes a highly reactive microglial subset. Brain Behav Immun. 2025;123:466–82.
58. Ju H, et al. Phagocytosis converts infiltrated monocytes to microglia-like phenotype in experimental brain ischemia. J Neuroinflammation. 2022;19(1):190.
59. Zhang Y, et al. Arresting the bad seed: HDAC3 regulates proliferation of different microglia after ischemic stroke. Sci Adv. 2024;10(10):eade6900.
60. Nauck MA, et al. GLP-1 receptor agonists in the treatment of type 2 diabetes - state-of-the-art. Mol Metab. 2021;46:101102.
61. Shan Y, et al. The glucagon-like peptide-1 receptor agonist reduces inflammation and blood-brain barrier breakdown in an astrocyte-dependent manner in experimental stroke. J Neuroinflammation. 2019;16(1):242.
62. Holst JJ. The physiology of glucagon-like peptide 1. Physiol Rev. 2007;87(4):1409–39.
63. Flint A, et al. Glucagon-like peptide 1 promotes satiety and suppresses energy intake in humans. J Clin Invest. 1998;101(3):515–20.
64. Sourris KC, et al. Glucagon-like peptide-1 receptor signaling modifies the extent of diabetic kidney disease through dampening the receptor for advanced glycation end products-induced inflammation. Kidney Int. 2024;105(1):132–49.
65. Muscogiuri G, et al. Glucagon-like Peptide-1 and the central/peripheral nervous system: crosstalk in diabetes. Trends Endocrinol Metab. 2017;28(2):88–103.
66. Lee YS, et al. Glucagon-like peptide-1 inhibits adipose tissue macrophage infiltration and inflammation in an obese mouse model of diabetes. Diabetologia. 2012;55(9):2456–68.
67. Tanaka M, et al. Differential effects of GLP-1 receptor agonist on foam cell formation in monocytes between non-obese and obese subjects. Metabolism. 2016;65(2):1–11.

Publisher's note